The Characterization of Atomically Precise Nanoclusters Using X-Ray Absorption Spectroscopy

5

Lisa Bovenkamp-Langlois and Martha W. Schaefer

Contents

L. Bovenkamp-Langlois (✉)
CAMD (Center for Advanced Microstructures and Devices), Louisiana State University, Baton Rouge, LA, USA

Center for Atomic-Level Catalyst Design, Cain Department of Chemical Engineering, Louisiana State University, Baton Rouge, LA, USA
e-mail: lbovenkamp@lsu.edu

M.W. Schaefer
CAMD (Center for Advanced Microstructures and Devices), Louisiana State University, Baton Rouge, LA, USA

Department of Geology and Geophysics, Louisiana State University, Baton Rouge, LA, USA

Department of Physics and Astronomy, Louisiana State University, Baton Rouge, LA, USA
e-mail: mws@lsu.edu

C.S.S.R. Kumar (ed.), *X-ray and Neutron Techniques for Nanomaterials Characterization*, DOI 10.1007/978-3-662-48606-1_5

1 Definition of the Topic

Overview of the methods and results of the application of X-ray absorption spectroscopy characterizing atomically precise nanoclusters.

2 Introduction

Interest in catalysts such as the atomically precise nanoclusters (APNCs) is growing. Much is still to be learned about the properties of these materials, however. At what point in cluster growth does a material change from the quantum behavior of a single atom or molecule to the ensemble behavior of a bulk metal [1]? Is the transition smooth with increasing cluster size, or is there an intermediate region where the clusters have properties that are neither metallic nor due to quantum size effects [2]? Is there a relationship between the size of the clusters and their electronic, optical, and catalytic properties [3]? Is there a correlation between structure and electronic properties [4]? How are structure and electronic properties affected by a complex environment (including different temperatures, pressures, or solvation effects) [5]? Since APNCs are the focus of this book, some answers to these questions are presented in other chapters.

However, a very brief introduction shall help the reader to understand the separation of the group of APNCs from the wider group of nanoparticles (NPs). The definition of NPs as mesoscopic systems between atoms or molecules and macroscopic bulk material can apply to a good number of structures with particle sizes of $\leq$ 100 nm. The term APNC means that these NPs have a precise number of atoms and generally implies that they are small (below 10 nm diameter). It is reported that the atomic precision of APNCs affects catalytic and optical properties and gives exceptional stability to the APNC (e.g., [4, 6–8]). A brief history of Au APNCs is given in Schaaff et al. [7].

The first step in understanding the correlation between the structure and the chemical and physical properties (which enable tailoring of the catalytic properties of the APNC [9]) is to gain precise knowledge about the structure of the clusters. X-ray diffraction (XRD) is the best method to determine the structure of a material. For APNCs, there is a certain degree of disorder [10] and fluidity [11] on the surface due to the presence of ligands. For this reason, it is mostly not possible to grow crystals and determine the structure using XRD [12]. In order to find some understanding of the structure for these cases, certain semiempirical models have been developed [13, 14]. For example, "staple fitness," concerning the highest structural stability of the staple motif [15], will be discussed later in this paper.

The most basic structural models were created on the basis of atomic packing structures (e.g., fcc) and are summarized by Benfield [16]. The atomic packing mode in metal NCs is in direct correlation with their size and other structural properties [4, 9, 17]. Specifically, the stability stands in direct relation to the so-called magic numbers [9]. Details will be discussed further below. New approaches using density functional theory (DFT) have made it possible to determine the structures of several

clusters, e.g., $Au_{25}(SR)_{18}$ [18], $Au_{38}(SR)_{24}$ [19], and $Au_{144}(SR)_{60}$ [20]. Challenges include the determination of the cluster size (more specifically the number of atoms) from the packing mode models and the understanding why smaller clusters have icosahedral structure in one case and cuboctahedral structure in another [11].

The most studied group among the APNCs is the gold clusters ($Au_x(SR)_y$) with thiol capping. This is because when the gold–sulfur interface can be understood (including atomic and electronic structure, properties of signal transmittance, excitations, and electron transport), then they can be applied to fields such as nanocatalysis, molecular electronics, biolabeling, photonics, and sensing [20]. Further, the extremely high surface-to-volume ratio of these gold clusters ($Au_x(SR)_y$) can help with the understanding of self-organization processes in self-assembled monolayers (SAM) [7]. Solution phase investigations of Au clusters can reveal the physical and chemical properties of atomically precise Au nanoclusters [21]. In contrast to the use of thiol ligands is a new method of NC stabilization with s: These dendrimer-encapsulated nanoclusters (DENs) show quite different properties compared to thiol-stabilized NCs [22].

The second step in the understanding of the physical and chemical properties (specifically the catalytic properties) of APNCs is the determination of their electronic properties, which depend on the basic structure (size, packing) and environment. In particular, the size of a cluster will determine whether its electronic properties are discrete, i.e., atoms, molecules, and small clusters or form a band structure, i.e., bulk metals [4]. Common techniques to determine the electronic structure of materials are UV–vis spectroscopy and X-ray photoelectron spectroscopy (XPS) (which needs ultrahigh vacuum (UHV) conditions [9]). Another procedure that is used is the calculation of density of states based on quantum chemistry [23].

The goal of the generation of APNC is not only the control of the size (e.g., number of atoms) but also the distribution of metals in the case of the bimetallic NC. The determination of the distribution of the two metals is another aspect of the concept of "active sites" which includes defects, sharp corners, and atomic steps, and its understanding can help control catalytic reactions further [6].

The electronic properties can change if the two metals are distributed in the certain way [24]. For example, alloys with Pd, Ag, Pt, or Cu based on $Au_{25}(SR)_{18}$ and $Au_{38}(SR)_{24}$ NC were synthesized and investigated by both theory and experiment and showed that the content and distribution of second metal (doping) have direct effects on the geometrical structure and electronic properties (e.g., [25–28]). In the cases of $Au_{24}Pt(SR)_{18}$ [25], $Au_{24}Ag(SR)_{18}$ [26], $Au_{24}Pd(SR)_{18}$ [27, 28], and $Au_{24}Cu(SR)_{18}$ [29, 30], the dopant atoms are believed to occupy the central site of the metal core. It is the precise knowledge of the structure and electronic properties of the NCs that is important in the understanding of the catalytic properties. To achieve this goal, methods to investigate the structure and electronic properties have to be developed constantly [31].

A powerful characterization technique for many materials is X-ray absorption spectroscopy (XAS). XAS has become a very important tool among the synchrotron-based techniques for the characterization of materials, especially metal nanoparticles

and catalysts [9, 32]. Because XAS is element specific, this gives a very special opportunity to observe the same sample from different points of view if several elements, e.g., metals in alloy, are used (more details below). XAS is applicable to a broad range of elemental concentrations (i.e., from tens of ppm to wt% levels) [32] for solids and liquids as well and does not require long-range order in the sample [33]. In addition to the oxidation state, the chemical environment and geometrical information can be extracted from XAS. One aspect of XAS that especially combines theoretical and experimental techniques is extended X-ray absorption fine structure (EXAFS) spectroscopy. The analysis of EXAFS can:

- Determine coordination numbers (CN) to the neighboring atoms in a NC
- Determine distances of Me–Me and Me–L bonding
- Compare structure models with experimental data
- Determine structural disorder (up to a degree)

These important structural details can even be extracted from amorphous materials [2]. The resolution of EXAFS regarding the bond distances is of the order of 0.001 Å within a distance of about 10 Å from the center to analyze the local structure [3]. In this respect, EXAFS can even extract structural information which is based on the atomic packing models above from systems that do not have a long-range order.

Using the other aspect of XAS, X-ray absorption near-edge structure (XANES, formerly called NEXAFS) spectroscopy, it is possible to:

- Analyze the electronic properties (i.e., density of electronic states above the Fermi level)
- Determine the effective oxidation state
- Determine the chemical speciation

In this review, we focus on the methods and problems that are connected with the characterization of APNCs using XAS. Correct structural models and purity of NP content are the most important aspects to highlight. Together EXAFS and XANES are very versatile (nondestructive, study both atomic and electronic structure) and can be applied to the characterization of all kinds of materials and reactions in situ, even if they require high temperatures, high pressures, or other environmental changes, e.g., solvation and vaporization [12]. XAS techniques can be combined with theoretical calculations to validate structural models [31].

Some questions that will be answered in this review are the following:

- When was EXAFS first used for the characterization of APNC?
- How is the atomic size (numbers of atoms) determined by using EXAFS?
- What is so different in the use of EXAFS to study APNC compared to normal NP?
- What is the effect of structural disorder on the EXAFS analysis technique?
- How can the electronic information contained in XANES be extracted?

This latest review focuses on the use of XAS to characterize the structure, electronic properties, and behavior of APNCs, including during heating, solvation, and catalytic activity.

Other recent reviews on related topics include the following: Bare and Ressler [32] and Frenkel et al. [34] discuss the broader field of catalysis and the application of catalytic reactors together with (in situ) XAS. A more specified discussion of the catalytic activity of metal DENs using catalytic reactors investigated with in situ XAS was published by Myers et al. [22]. The wider region of the characterization of NP using XAS was reviewed by Frenkel et al. [35], Lapresta-Fernandez et al. [36], and Modrow [9].

In the wide field of applications of EXAFS, theoretical methods especially the combination of EXAFS with other theoretical methods such as density functional theory (DFT) and molecular dynamics (MD) are progressing fast and are becoming the state of the art of the characterization techniques [34]. Some of these techniques will be discussed here later to present a complete as possible overview of the techniques currently available in the XAS toolbox.

The evolution of clusters from atomic to bulk including both theoretical and experimental discussions is found in Schmid [37]. The interplay of atomic and electronic structure from a more theoretical point of view is discussed by Hakkinen [38] and Pei and Zeng [39].

Frenkel [40] and Gao and Goodman [41] discussed the specifics of the characterization of bimetallic NP, while Jin and Nobusada [42] focused on the methods of alloying within NCs with respect to different elements. Zhang [43] summarized the research on gold APNCs that was done in his group using XAS methods in a very recent review. Zhang also sketched very briefly using excellent illustrations the advantages and results that can be drawn from XAS. There can be found many more reviews on the different aspects of APNC. However, these do not mention the characterizational strength of the XAS toolbox.

The sections of this chapter are organized as follows: A short introduction of the physics of XAS and the specifics of XANES and EXAFS is followed by a discussion of the experimental setup in the next section. The main section of this chapter discusses the techniques of the application of first, EXAFS and second, XANES that are used in order to gain structural and electronic information from investigations of APNCs and the key findings.

3 Experimental and Instrumental Methodology

3.1 The Physics of X-Ray Absorption Spectroscopy

X-ray absorption spectroscopy (XAS) is a sophisticated tool to analyze many different types of materials. It is especially useful because no long-range order is required, but only the local environment of the element of interest is significant. This qualifies XAS as an excellent tool for the investigation of noncrystalline systems.

The analysis of XAS spectra can give details on oxidation state, geometry, and the kinds of neighboring atoms. The element under investigation can be chosen because of the distinct electron binding energies. There are a number of introductory texts on XAS available in the literature, for example, Bunker [44], Calvin [45], Kelly et al. [46], Koningsberger, Prins [33], and Teo [47]. In a nutshell: The law of Lambert–Beer

$$I = I_0 e^{-\mu_l(E)x} \tag{5.1}$$

describes the attenuation of radiation of initial intensity I_0 with regard to intensity I at a distance x within a material. $\mu_l(E)$ (short, μ) is the linear absorption coefficient at energy E. For XAS experiments, bonding energies of inner shell electrons extend from UV light for light elements (≈50 eV) up to hard X-rays (≈100 keV) for heavy elements. In this typical energy range for XAS experiments, the absorption coefficient μ is dominated by the photoelectric effect. XAS involves the measurement of the absorption coefficient μ as a function of photon energy E close to the ionization energy of an inner shell electron in a material and reveals a fine structure (see Fig. 5.1). The energy at which the absorption rises abruptly is called the absorption edge, and the energetic position is denoted E_0. This fine structure is an oscillatory structure that modulates the (atomic) absorption coefficient of an isolated atom and originates from the interaction of an electron excited by photo absorption with the surrounding material. In the quantum mechanical picture of the photoelectron as a matter wave, the oscillatory structure can be explained as interference between waves, one wave leaving the absorbing atom and the other waves that are backscattered from the neighboring atoms according to the scattering effects of the chemical environment. Because electron binding energies are element specific, XAS is element specific.

The non-modulated absorption coefficient μ_0, related to an environment where no neighboring atoms are present, is called the atomic background. The atomic background can be approximated by an arc tangent curve but is, mostly, masked by the features of the main edge (cf. Fig. 5.1). Materials that can be examined with XAS are solids, fluids, or gases. XAS is divided into two aspects depending on the involvement of the type of scattering contribution and molecular orbitals to the signal. X-ray absorption near-edge structure (XANES) spectroscopy is the part of the fine structure close to the absorption edge E_0 (typical −20 eV to 50 eV with respect to E_0) showing intense features. In addition to the oxidation state, the chemical environment and geometrical information can be extracted from XANES using the fingerprinting technique. The XANES region is dominated by multiple scattering and transitions into molecular orbitals. The extended X-ray absorption fine structure (EXAFS) region extends out to 1000 eV above E_0 and is mainly contributed by single scattering. The analysis of the EXAFS signal provides local structural information such as distance and CN of neighboring atoms. The information contained in a XAS spectrum is averaged over all atoms (of the element under investigation) that are probed (i.e., the atoms within the sample that are hit by the photon beam).

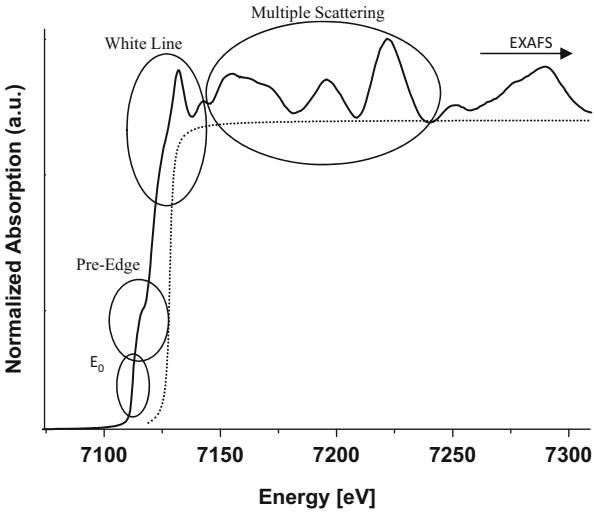

Fig. 5.1 Fe K-XANES spectrum of metallic iron (—) and the atomic background (. . .)

3.2 XANES

The fine structure of the near-edge (XANES, earlier NEXAFS) spectra consists of distinct characteristics such as pre-edge peaks, a white line (WL), shape resonances (SR), and the energy position of the absorption edge E_0 (cf. Fig. 5.1). The position of the edge E_0 is usually defined as the inflection point in the main rise of μ(E). In cases such as transition metals (Ti, Co, Fe, and so on), this position can be masked by pre-edge features. Figure 5.1 shows an example for iron metal. The position of the absorption edge E_0 can shift due to the oxidation state of the absorbing atom or electronegativity of the neighboring atoms [48]. The white line (WL) is named after the strong feature just above the absorption edge which was observed in photosensitive films used to record spectra in early XAS experiments. Pre-edge features and WL peaks arise from transitions into unoccupied atomic or molecular orbitals (MO) above the Fermi level. All other features after the WL (up to about 50 eV) are called shape resonances (SR). SR are also characteristic features, and they have their origin in multiple scattering with neighboring atoms. Together the shape and position of each of the characteristic features in the XANES spectrum comprise a fingerprint of the electronic and geometric environment of the absorbing element. This chemical environment can be determined by comparison to XANES spectra of compounds with known structures.

Additional information contained in the XANES spectrum comes from the correlation of the WL feature to molecular orbitals and density of states [33]. The density of states (DOS) describes the number density of available states as a function of energy [49]. Further, the l-projected DOS (l-DOS) only includes the DOS for a specific quantum number ($l = 0, 1, 2$, etc.) which corresponds to the classification of the orbitals due to their angular momentum (s, p, d, respectively). The shape of a

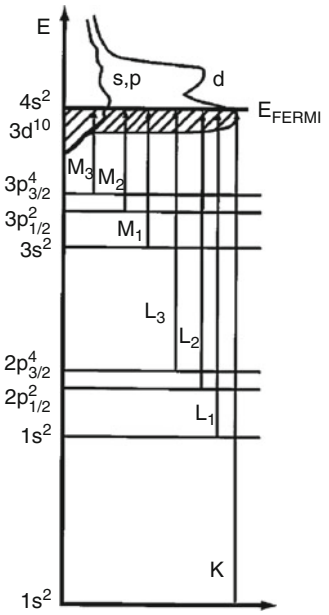

Fig. 5.2 The density of states (DOS) depicted on the top reflects the transitions of electrons from core levels into unoccupied states above the Fermi energy (E_{FERMI}). The transitions starting from specific core levels correspond to the absorption edges of XAS (Reprinted with permission from Rehr and Albers [50]. Copyright 2000 by the American Physical Society)

XANES spectrum reflects the projected electronic DOS of excited states because the XANES "function" $\chi(E)$ and the l-DOS $\rho(E)$ share the same fine structure:

$$\rho(E) = \rho_0(E)\,[1 + \chi(E)] \tag{5.2}$$

Here, E is the photoelectron energy, and $\rho_0(E)$ is the density of states for the atomic background [50]. The XANES spectrum is derived from the reflection of transitions into unoccupied states above the Fermi level. Figure 5.2 depicts the relationship between the transitions from core states and the absorption edges (K, L, M).

To correlate the unoccupied l-DOS $\rho(E)$ with experimental XANES, the relation

$$\rho(E) = [\rho_0(E)/\mu_0(E)]\,\mu(E) \tag{5.3}$$

can be used, where $\mu_0(E)$ describes the effects of the core–hole interaction. In general, unoccupied states show up as peaks (reflecting possible transitions between molecular orbitals), and hybridization of orbitals is revealed when peaks in different orbitals have the same energy [9].

3.3 EXAFS

More than 50 eV up to 1000 eV above the absorption edge (E_0), the fine structure is much reduced in intensity but not reduced in information content. Therefore, in order to extract the information, the smooth atomic background has to be removed, and $\chi(E)$, the fine structure function (Fig. 5.3), is calculated:

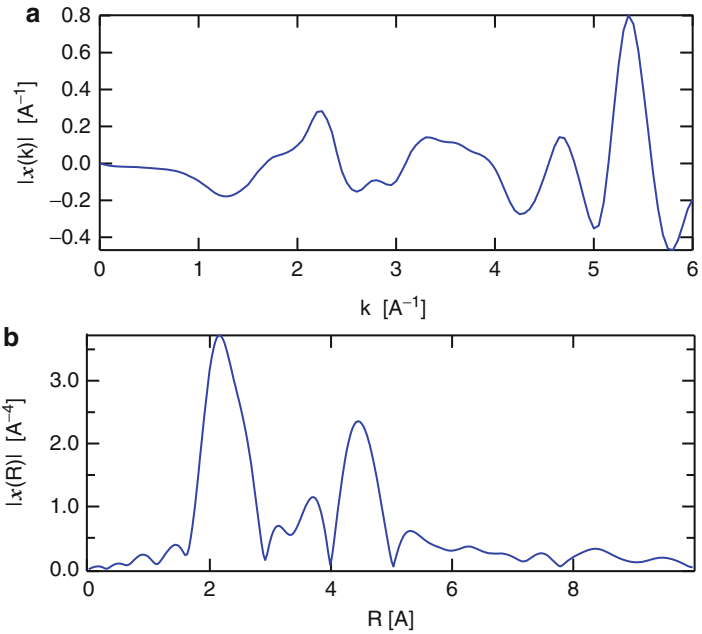

Fig. 5.3 Fine structure of the Fe metal EXAFS spectrum (**a**) $\chi(k)$ and (**b**) Fourier transformed, $\chi(R)$

$$\chi(E) = \frac{\mu(E) - \mu_0(E)}{\Delta\mu(E)} \tag{5.4}$$

where $\mu(E)$ is the measured absorption coefficient, $\mu_0(E)$ is the atomic background (a function calculated as a spline), and $\Delta\mu(E)$ is the edge step. Further, this function of the oscillations is converted into k-space using $k^2 = 2\,m/\hbar^2(E - E_0)$ (with m, the mass of the electron, and $\hbar$, the Planck constant (over 2π)) and using Fourier transformation into R-space (Fig. 5.3).

The interference between initial and backscattered waves as well as some examples for scattering paths is visualized in Fig. 5.4. Two main types of scattering paths are distinguished: single scattering and multiple scattering. Single scattering is in general sufficient to calculate the EXAFS part of the spectrum with the addition of some corrections regarding multiple scattering. Single scattering occurs only if the wavelength of the outgoing photoelectron wave λ is smaller than the interatomic bond distance R. Usually, this refers to a value of about +50 eV above E_0.

The EXAFS function $\chi(k)$ is directly connected to the parameters of the environment of the absorbing atom. These parameters are described in the EXAFS equation [50]:

$$\chi(k) = \sum_R S_0^2 N_R \frac{|f(k)|}{kR^2} * sin\,(2kR + 2\delta_c + \Phi) e^{-2R/\lambda(k)} e^{-2\sigma^2 k^2} \tag{5.5}$$

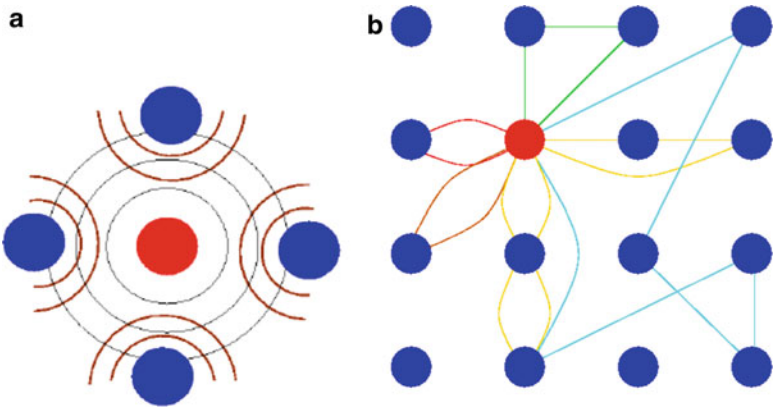

Fig. 5.4 (**a**) The interference between the outgoing wave and the backscattered waves is the source of the oscillatory structure in EXAFS, (**b**) examples for single scattering (*red*, *brown*) and multiple scattering paths (*green, yellow, blue*) in a crystal (From Ravel [51], used with permission)

where $\chi(k)$ represents the pure oscillations in k-space. S_0^2 is a factor that includes inelastic losses, N_R is the CN of neighbors at a certain radius, $f(k)$ is the scattering amplitude, R is the distance to the neighboring atoms, δ_e is the phase shift, λ is the mean free path for inelastic losses, and σ^2 is the Debye–Waller factor which relates to thermal and structural disorder. In order to extract the contributions of different backscattered waves, a Fourier transformation is performed, usually denoted FT $\chi(k)$ or just $\chi(R)$. From these parameters, bond lengths and coordination numbers can be extracted.

At present, EXAFS data are analyzed by refining the theoretically calculated EXAFS spectra of single paths using the sum of path rule:

$$\chi(k) = \sum_P \chi_P(k) \tag{5.6}$$

where χ_P denotes each path contributing to the spectrum.

The modern analysis of EXAFS data is done with programs such as Artemis (Demeter/Ifeffit) [52], WinXAS [53], or GNXAS [54]. The details of the application of these methods are described there. Briefly, the EXAFS spectrum in k-space is fitted using theoretically calculated scattering amplitudes and phase shifts from reference compounds with known structure. The parameters of the EXAFS equation are set as a relation to the structural values given for the known compounds. For the analysis of the EXAFS data, especially in the case of NCs, it is very important that the samples are 100 % NC and not containing by-products or precursors that contain the element under investigation [55]. For an EXAFS fit, it is important to have a model for the structure that is to be characterized. In the case of metallic NC, this model as a first-order approximation can be the metallic bulk structure. With a fit, distance and CNs with the first neighbors (up to five shells) are determined with the use of information about the Au–Au distance and CNs derived from the metal bulk.

The number of SS paths (also coordination numbers) and the number of multiple scattering paths are intercorrelated and depend on the size and shape of the crystallites (i.e., the NC).

For the EXAFS fitting approach for NP, the following constraints have been proposed previously [35, 56–59]:

1. The degeneracy of multiple scattering paths has to be optimized within a range obtained by the measured size distribution of the nanoparticles.
2. Due to the presence of surface, i.e., ill coordinated, atoms in NP systems, the bond distance and bond–angle distributions are affected; therefore, it must be possible to determine the bond distances separately from the bulk metal system.
3. Because the background is the same as in bulk crystalline metal foil, nonstructural parameters are fixed to the values obtained for bulk metal within their estimated uncertainty (S_O^2, ΔE_0).

The EXAFS analysis of bimetallic APNCs is even more challenging [55]. For alloy nanoclusters, the further following constraints are used on the heterometallic bonds based on Nashner et al., Frenkel, and Knecht et al. [40, 60–62]:

1. The CNs ($N_{Me1\text{-}Me2}$ and $N_{Me2\text{-}Me1}$ are heterometallic coordination numbers) of the *Me–Me* bonds for the two different metals (*Me1* and *Me2*) have to relate to their concentration c: $N_{Me1-Me2}/N_{Me2-Me1} = c_{Me2}/c_{Me1}$.
2. The distances R between atoms of the two metals in each shell have to be the same: $R_{Me1-Me2} = R_{Me2-Me1}$.
3. The disorder parameters (Debye–Waller factor, σ^2) for both metals in each shell have to be the same: $\sigma^2{}_{Me1-Me2} = \sigma^2{}_{Me2-Me1}$.

3.4 The XAS Experiment

Synchrotron radiation is monochromatized using a set of parallel crystals in a double crystal monochromator applying Bragg's law:

$$n \cdot \lambda = 2 \cdot d \cdot \sin\theta \tag{5.7}$$

with n being the order number, λ the wavelength of the reflected light, d the spacing of the crystal, and θ the Bragg angle. Slits are used to collimate and mirrors to focus the incoming beam onto the sample position.

A double crystal monochromator with parallel crystal setup is preferred for XAS experiments because the incoming and exiting beams are parallel to each other [63]. This way the monochromatized beam is fixed on the sample position, while the energy is scanned. The rest of this experimental setup consists of ionization chambers to measure the photon current before and after the sample and of an energy-dispersive semiconductor detector, positioned at a 90° angle with respect to

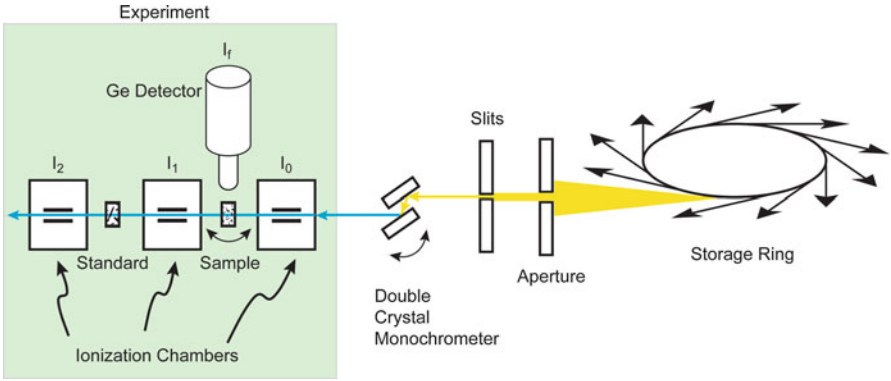

Fig. 5.5 Experimental setup of a XAS experiment

the incoming beam, to measure fluorescence photons coming from the sample. The layout is displayed in Fig. 5.5.

After monochromatizing, the photons pass through the two ionization chambers and the sample to measure $\mu(E)$. For concentrated samples, the absorption μ can be measured indirectly by applying the law of Lambert–Beer (cf. Eq. 5.1) – transmission mode:

$$\mu(E) \propto ln\left(\frac{I_0}{I_1}\right) \tag{5.8}$$

The absorption coefficient $\mu(E)$ is determined by measuring the photon current before the sample (I_0) and behind the sample (I_1). If another ionization chamber (I_2) is installed behind I_1, a standard (e.g., metal foil) can be measured at the same time with the sample. This standard is used for energy calibration purposes.

Diluted samples with less than 1 % concentration of the absorbing element are measured in fluorescence mode where the semiconductor detector collects the fluorescence photons (I_f) that are emitted as response to the absorption of the incident beam (I_0) by the sample. Fluorescence and Auger electrons are the two relaxation mechanisms of atoms excited by X-ray radiation. For fluorescence detection, the absorption coefficient $\mu(E)$ is described by

$$\mu(E) \propto \left(\frac{I_f}{I_0}\right) \tag{5.9}$$

Equation 5.9 is an approximation and only valid if the sample is thin and diluted so that no self-absorption occurs. Also, the sample should face in the direction of 45° with respect to the incoming beam (and therefore also the semiconductor detector) [44].

The sample preparation can have significant effects on the measurement. It is important that the samples are of the right average thickness and are homogeneous.

The thickness of the sample determines the total absorption, which ideally should be about 1. Homogeneity of the sample is important because a nonhomogeneous sample will have a distribution of absorption coefficients instead of a well-characterized single value. As discussed by Lee et al. [64] and Stern and Kim [65], if samples have, for example, little holes, the absorption coefficient cannot be the same at each point (see Eq. 5.1). Therefore, if the absorption coefficient μ is not measured correctly, the data evaluated from those measurements cannot be reliable, especially for the increased distortions in monocrystalline materials due to higher surface-to-volume ratio [66, 67].

4 Key Research Methods and Findings on APNCs Characterized Using XAS

4.1 EXAFS

The EXAFS analysis method is very important for the characterization of metal clusters and catalysts. EXAFS analysis is used to determine specific information about materials including the chemical identity, average bond lengths for the different shells, and ensemble-average CN of atoms in each shell around a central atom. To date, only APNCs containing Au, Pd, Pt, and some alloys (e.g., Au–Cu, Au–Pd, and Au–Pt) have been characterized by EXAFS. The literature reporting EXAFS used for the characterization of APNCs together with the details of the EXAFS analyses is summarized in Table 5.1.

4.1.1 Simple Structural Models

The first reports of the characterization of APNCs with EXAFS, i.e., Au_{55} clusters made by the Schmid [68] process by Cluskey et al. [69], Fairbanks et al. [70], and Marcus et al. [71], used early EXAFS analysis techniques where experimental phase shifts and amplitude of reference materials were compared with those of the unknown sample, and the software to make use of the EXAFS equation was just beginning to be developed. With time, a more complete understanding of the various effects that impact the spectra and the improvement of the analysis software has made possible a much more sophisticated approach to the analysis of EXAFS spectra. Better understanding of the effect of multiple scattering and curved wave effects [72] has improved the characterization of APNC with EXAFS. Early EXAFS results on Pd_{561} [72] and also Au_{55} [10] were revised and refined.

Several papers on the characterization of nanoparticles (not APNC) using EXAFS [17, 57–59, 73] form the basis for reliable results derived from EXAFS. In these publications, Frenkel and coworkers discuss the importance of multiple scattering effects [58] on the EXAFS analysis and models regarding the structural geometry of the nanoclusters [17, 59, 73], summarized in Frenkel et al. [35]. Together with the development of the FEFF code (specifically version 6), the calculation of multiple scattering paths became possible. This big improvement boosted the development of analysis software (e.g., WinXAS [53], Ifeffit, and Demeter [52]). The analysis of

Table 5.1 Summary of EXAFS data on APNCs

Nanocluster	EXAFS	1st shell M–M CN	1st shell M–M dist., r (Å)	Disorder param (10^{-3} Å^2)	Other shells, dopant data	Structure	k-range (Å^{-1})	EXAFS fit plot?	Other techniques	Reference
GOLD										
$Au_{11}\{PPh_2(p\text{-}ClC_5H_4)\}_7I_3$ (80 K)	Au L_3-edge	1.4 ± 2	2.66 ± 0.01	4 ± 6	2nd Au-Au: CN = 2.4 ± 1, r = 2.87 ± 0.02	–	–	No	None	Clusky et al. 1993 [69]
					3rd Au-Au: CN = 3.2 ± 3, r = 4.68 ± 0.03					
					Au-P: CN = 0.8 ± 1, r = 2.27 ± 0.04					
					Au-I: CN = 2.6 ± 2, r = 2.64 ± 0.07					
$Au_{13}[PPh_3]_4[S(CH_2)_{11}CH_3]_2Cl_2$ $Au_{13}[PPh_3]_4[S(CH_2)_{11}CH_3]_4$ (not distinguished in results)	Au L_3-edge	6.5 ± 0.5	–	–	2nd Au-Au: CN = 0	–	–	Yes	XANES, HAADF-STEM, TEM	Frenkel et al. 2007 [89]
					3rd Au-Au: CN = 5 ± 1					
					Au-S: CN = 0.72 ± 0.05					
$Au_{13}[PPh_3]_4[S(CH_2)_{11}CH_3]_2Cl_2$	Au L_3-edge	SS1 path: 6.2 ± 0.6	SS1 path: 2.83 ± 0.01	Au-Au: 14 ± 1	TR path: CN = 34 ± 26, r = 4.24 ± 0.05	–	3-12	Yes	XANES, HRTEM, HAADF-STEM	Menard et al. 2006 [3]
					SS3 path: CN = 8 ± 6, r = 4.75 ± 0.03					
				Au-S: 5 ± 1	Au-S SS1 path: CN = 0.83 ± 0.08, r = 2.310 ± 0.007					

$Au_{13}[PPh_3]_4[S(CH_2)_{11}CH_3]_4$	Au L_3-edge	SS1 path: 6.7 ± 0.7	SS1 path: 2.85 ± 0.02	Au-Au: 15 ± 1	TR path: CN = 21 ± 8, r = 4.26 ± 0.03	–	3-12	Yes	(As above)	Menard et al. 2006 [3]
					SS3 path: CN = 8 ± 4, r = 4.75 ± 0.02					
				Au-S: 3 ± 1	Au-S SS1 path: CN = 0.76 ± 0.07, r = 2.324 ± 0.007					
Au_{13} P2VP in solution (P2VP = polystyrene-2-vinylpiridine)	Au L_3-edge	9.4	2.84 ± 0.01	12 ± 1	Au-X: CN = 0.2, r = 2.09 ± 0.03	–	2-12	Yes	XANES, FEFF DFT, XPS, HAADF-STEM, AFM	Behafarid et al. 2014 [106]
Au_{13} P2VP on Al_2O_3 (P2VP = polystyrene-2-vinylpiridine)	Au L_3-edge	8.2	2.79 ± 0.01	15 ± 2	Au-X: CN = 0.7, r = 2.11 ± 0.02	–	2-12	Yes	(As above)	Behafarid et al. 2014 [106]
$Au_{19}(SR)_{13}$	Au L_3-edge	1.05*	2.83 ± 0.01	4 ± 1	2^{nd} Au-Au: CN = 1.89*, r = 3.04 ± 0.02	Icosahedral	2.5–11.5	Yes	XANES, XPS	Chevrier et al. 2012 [95]
					3^{rd} Au-Au: CN = 1.89*, r = 3.37 ± 0.03					
					Au-S: CN = 1.37*, r = 2.33 ± 0.01					
$Au_{22}(SG)_{18}$	Au L_3-edge	0.7	2.67 ± 0.01	–	Au-S: CN = 1.7, r = 2.314 ± 0.004	Face-centered cubic	3.0–13.5	Yes	XANES, XPS	Yu et al. 2014 [146]
$Au_{24}Pt(SR)_{18}$	Pt L_3-edge	–	–	10 ± 1	Pt-S: CN = 2.6 ± 0.1, r = 2.319 ± 0.004	Icosahedral	3–8.8	No	MALDI, XPS, l-DOS	Christensen et al. 2012 [25]
					Pt-Au: CN = 5.5 ± 0.3, r = 2.750 ± 0.004					

(*continued*)

Table 5.1 (continued)

Nanocluster	EXAFS	1st shell M–M CN	1st shell M–M dist., r (Å)	Disorder param (10^{-3} Å^2)	Other shells, dopant data	Structure	k-range (Å^{-1})	EXAFS fit plot?	Other techniques	Reference
$Au_{24}Pt(SR)_{18}$	Au L_3-edge	$2 \pm 1^{\epsilon}$	$2.79 \pm 0.01^{\epsilon}$	13 ± 5	Au-S: CN = 1.7 ± 0.2, r = 2.315 ± 0.005	Icosahedral	3-12	Yes	(As above)	Christensen et al. 2012 [25]
$Au_{24}Pd(SC_{12}H_{25})_{18}$	Pd K-edge	–	–	–	Pd-Au: CN = 10.7 ± 0.9 r = 2.750 ± 0.005	–	3-15	No	None	Negishi et al. 2013 [28]
Au_{25}	Au L_3-edge	1.1 ± 0.2	2.81 ± 0.01	6 ± 1	Au-S: CN = 1.6 ± 0.1, r = 2.332 ± 0.007	Icosahedral	3-12	Yes	MALDI, XPS, l-DOS	Christensen et al. 2012 [25]
$[Au_{25}(TePh)_{\sim 3}(SC_8H_{17})_{\sim 15}]^-$	Au L_3-edge	0.9 ± 0.9	2.782 ± 0.025	1.0 ± 8.4	Au-S: CN = 1.4 ± 0.3, r = 2.299 ± 0.007 Au-Te: CN = 0.3 ± 0.2, r = 2.579 ± 0.019	–	3-15	No	XANES, ESI/MALDI, TEM, UV–vis	Kurashige et al. 2014 [110]
$[Au_{25}(TePh)_{\sim 7}(SC_8H_{17})_{\sim 11}]^-$	Au L_3-edge	1.0 ± 0.9	2.774 ± 0.031	0.6 ± 0.6	Au-S: CN = 1.2 ± 0.3, r = 2.299 ± 0.013 Au-Te: CN = 0.8 ± 0.3, r = 2.589 ± 0.013	–	3-15	No	(As above)	Kurashige et al. 2014 [110]
$[Au_{25}(PPh_3)_{10}(SC_{12}H_{25})_5Cl_2]^{2+}$ Au_{25}–*bi*	Au L_3-edge	6.9 ± 1.3	2.82 ± 0.03	–	Au-S: CN = 0.7 ± 0.4, r = 2.30 ± 0.05	Bi-icosahedral	2-11.5	No	XANES, UPS	Liu et al. 2013 [115]
$[Au_{25}(SCH_2CH_2Ph)_{18}]^-$ Au_{25}-*i*	Au L_3-edge	4.8 ± 1.3	2.80 ± 0.04	–	Au-S: CN = 1.2 ± 0.4, r = 2.30 ± 0.04	Icosahedral	2–11.5	No	(As above)	Liu et al. 2013 [115]

$[Au_{25}(SC_8H_{17})_{18}]^-$	Au L_3-edge	0.7 ± 0.5	2.738 ± 0.011	0.5 ± 3.3	Au-S: CN = 1.6 ± 0.2, r = 2.309 ± 0.003	–	3-15	No	XANES, ESI/MALDI, TEM, UV–vis	Kurashige et al. 2014 [110]
$Au_{(25)}$-BSA (BSA = bovine serum albumin)	Au L_3-edge	3.0 ± 0.4	2.81 ± 0.01	10 ± 1	Au-S: CN = 1.2 ± 0.1, r = 2.30 ± 0.01	Icosahedral	3-12	Yes	XANES, XPS, TEM	Simms et al. 2009 [84]
[TOA] + $[Au_{25}(SCH_2CH_2Ph)_{18}]^-$ (TOA = tetraoctylammonium)	Au L_3-edge	1.44*	300 K: 2.82 ± 0.01 10 K: 2.80 ± 0.01	300 K: 8.4 10 K: 4.9	2^{nd} Au-Au, 300 K: r = 2.97 ± 0.01, 10 K: r = 2.97 ± 0.01	Icosahedral	3-12	Yes	XANES, l-DOS	MacDonald et al. 2011 [5]
					3^{rd} Au-Au, 300 K: r = 3.14 ± 0.02, 10 K: r = 3.20 ± 0.02					
					Au-S, 300 K: r = 2.32 ± 0.01, 10 K: r = 2.32 ± 0.01					
Solvated [TOA] + $[Au_{25}(SCH_2CH_2Ph)_{18}]^-$ (TOA = tetraoctylammonium) (a) Toluene (b) ACN = actetonitril	Au L_3-edge	1.44*	in toluene: 2.79 ± 0.01	in toluene: 7.4	2^{nd} Au-Au, in toluene: r = 2.95 ± 0.01, in ACN: r = 2.95 ± 0.01	Icosahedral	3-12	Yes	(As above)	MacDonald et al. 2011 [5]
			in ACN 2.79 ± 0.01	in AC: 7.2	3^{rd} Au-Au, in toluene: r = 3.19 ± 0.02, in ACN: r = 3.14 ± 0.02					
					Au-S, in toluene: r = 2.33 ± 0.01, in ACN: r = 2.32 ± 0.01					

(*continued*)

Table 5.1 (continued)

Nanocluster	EXAFS	1st shell M–M CN	1st shell M–M dist., r (Å)	Disorder param (10^{-3} Å^2)	Other shells, dopant data	Structure	k-range (Å^{-1})	EXAFS fit plot?	Other techniques	Reference
$Au_{25}(SR)_{18}$	Au L_3-edge	300 K: 1.44*	300 K: 2.80 ± 0.01	300 K: 9 ± 1	300 K: Au-S: CN = 1.44*, r = 2.321 ± 0.005	Icosahedral	3-11.3	Yes	XANES, FEFF, l–DOS	Chevrier et al. 2014 [99]
$Au_{25}(SR)_{18}$	Au L_3-edge	300 K: 1.44*	300 K: 2.790 ± 0.005	300 K: 4.8 ± 0.5	300 K: Au-S: CN = 1.44*, r = 2.333 ± 0.002	Icosahedral	3-13	Yes	XANES, l-DOS	Chevrier et al. 2014 [96]
		50 K: 1.44*	50 K: 2.784 ± 0.006	50 K: 3.0 ± 0.4	2nd shell Au-Au: CN = 1.92*, r = 2.97 ± 0.01					
					3rd shell Au-Au: CN = 2.88*, r = 3.22 ± 0.06					
					50 K: Au-S: CN = 1.44*, r = 2.327 ± 0.003					
					2nd shell Au-Au: CN = 1.92*, r = 2.955 ± 0.08					
					3rd shell Au-Au: CN = 2.88*, r = 3.16 ± 0.01					

$Au_{25}(SeR)_{18}$	Au L_3-edge	300 K: 1.44*	300 K: 2.70 ± 0.01	300 K: 5.0 ± 1.0	300 K: Au-Se CN = 1.44*, r = 2.417 ± 0.009	–	3-13	Yes	(As above)	Chevrier et al. 2014 [96]
		50 K: 1.44*	50 K: 2.775 ± 0.009	50 K: 5.4 ± 0.7	2^{nd} shell Au-Au, 300 K: CN = 1.92*, r = 2.87 ± 0.02					
					3^{rd} shell Au-Au, 300 K: CN = 2.88*, r = 3.46 ± 0.04					
					50 K: Au-Se CN = 1.44*, r = 2.428 ± 0.004					
					2^{nd} shell Au-Au: CN = 1.92*, r = 2.98 ± 0.01					
					3^{rd} shell Au-Au: CN = 2.88*, r = 3.60 ± 0.03					
$Au_{25}(SeR)_{18}$	Se K-edge	–	no Au-Au/ no Se-Se	–	300 K: Au-Se: CN: 2, r = 2.408 ± 0.009	–	3-13	Yes	(As above)	Chevrier et al. 2014 [96]
					Se-C: CN: 1, r = 1957 ± 0.002					
					50 K: Au-Se: CN: 2.41 ± 0.01					
					Se-C: CN: 1, r = 1.87 ± 0.003					
CeO_2 rod supported $Au_{25}(SR)_{18}$ (SR = $-SCH_2CH_2Ph$)	Au L_3-edge	2-3	–	–	Au-S: CN~1, r = 2.31 (avg)	–	3-16	No	XANES, Raman, FTIR, MALDI-MS, HAADF-TEM	Wu et al. 2014 [91]

(*continued*)

Table 5.1 (continued)

Nanocluster	EXAFS	1st shell M–M CN	1st shell M–M dist., r (Å)	Disorder param (10^{-3} Å^2)	Other shells, dopant data	Structure	k-range (Å^{-1})	EXAFS fit plot?	Other techniques	Reference
Carbon-Supported $Au_{25}(SR)_{18}$ MPCs SR = Phenylethanethiolate	Au L_3-edge	25 °C: 1.44*	25 °C: 2.760 ± 0.002	25 °C: 7.9 ± 0.5	2nd Au-Au, 25 °C: CN = 1.92* r = 3.01 ± 0.02	Icosahedral	3–12.5	Yes	UV–vis, TEM, XPS, MALDI, TGA	Shivhare et al. 2013 [21]
		125 °C: 6.3 ± 0.5	125 °C: 2.848 ± 0.004	125 °C: 8.9 ± 0.5	3rd Au-Au, 25 °C: CN = 2.88*, r = 3.3 ± 0.1					
		150 °C: 7.3 ± 0.8	150 °C: 2.852 ± 0.003	150 °C: 8.9 ± 0.5	Au-S, 25 °C: CN = 2.0*, r = 2.32*					
		200 °C: 9.3 ± 0.3	200 °C: 2.855 ± 0.002	200 °C: 8.8 ± 0.2	Au-S, 125 °C: CN = 1.11 ± 0.09, r = 2.325 ± 0.004					
		250 °C: 10.1 ± 0.5	250 °C: 2.855 ± 0.002	250 °C: 8.6 ± 0.3	Au-S, 150 °C: CN = 0.75 ± 0.09, r = 2.331 ± 0.005					
					Au-S, 200 °C: CN = 0.63 ± 0.08, r = 2.342 ± 0.008					
					Au-S, 250 °C: CN = 0.5 ± 0.1, r = 2.33 ± 0.02					

Carbon Supported $Au_{25}(SR)_{18}$ MPCs SR = Hexanethiolate	Au L_3-edge	25 °C: 1.44*	25 °C: 2.805 ± 0.004	25 °C: 7.2 ± 0.2	2nd shell Au-Au, 25 °C: CN = 1.92*, r = 3.02 ± 0.01	Icosahedral	3–12.5	Yes	(As above)	Shivhare et al. 2013 [21]
		125 °C: 3.6 ± 0.3	125 °C: 2.855 ± 0.003	125 °C: 9.1 ± 0.5	3rd shell Au-Au, 25 °C: CN = 2.88*, r = 3.32 ± 0.02					
		150 °C: 6.7 ± 0.4	150 °C: 2.857 ± 0.005	150 °C: 8.4 ± 0.3	Au-S, 25 °C: CN = 1.8*, r = 2.315*					
		200 °C: 9.0 ± 0.7	200 °C: 2.851 ± 0.005	200 °C: 8.5 ± 0.5	Au-S, 125 °C: CN = 1.58 ± 0.06, r = 2.315 ± 0.002					
					Au-S, 150 °C: CN = 1.0 ± 0.1, r = 2.329 ± 0.006					
					Au-S, 200 °C: CN = 0.8 ± 0.2, r = 2.32 ± 0.02					
$Au_{28}(SR)_{20}$	Au L_3-edge	300 K: 1.71*	300 K: 2.732 ± 0.002	300 K: 5 ± 1	300 K: Au-S: CN = 1.43*, r = 2.322 ± 0.009	Face-centered cubic	3–11.3	Yes	XANES, FEFF, l-DOS	Chevrier et al. 2014 [99]
		90 K: 1.71*	90 K: 2.73 ± 0.01	90 K: 6 ± 1	2nd shell Au-Au: CN = 2.09*, r = 2.93 ± 0.03					
					90 K Au-S: CN = 1.43*, r = 2.328 ± 0.006					
					2nd shell Au-Au: CN = 2.09*, r = 2.99 ± 0.003					

(*continued*)

Table 5.1 (continued)

Nanocluster	EXAFS	1st shell M–M CN	1st shell M–M dist., r (Å)	Disorder param (10^{-3} Å^2)	Other shells, dopant data	Structure	k-range (Å^{-1})	EXAFS fit plot?	Other techniques	Reference
$Au_{36}(SR)_{24}$	Au L_3-edge	295 K: 2.06*	295 K: 2.732 ± 0.004	295 K: 8.0 ± 0.3	Au-S, 295 K: CN = 1.33*, r = 2.322 ± 0.002	Icosahedral	3–13.7	Yes	XANES, XPS, l-DOS	Chevrier et al. 2013 [98]
		90 K: 2.06*	90 K: 2.746 ± 0.003	90 K: 3.7 ± 0.9	2nd shell Au-Au, 295 K: CN = 2.56*, r = 2.89 ± 0.01					
					Au-S, 90 K: CN = 1.33*, r = 2.329 ± 0.002					
					2nd shell Au-Au, 90 K: CN = 2.56*, r = 2.951 ± 0.005					
$Au_{38}(SCH_2CH_2Ph)_{24}$ (solid)	Au L_3-edge	3.3*	2.789 ± 0.007	7.4 ± 0.8	Au-S: CN = 1.26*, r = 2.325 ± 0.004	Icosahedral	3–12.5	No	XANES, l-DOS	MacDonald et al. 2011 [85]
$Au_{38}(SCH_2CH_2Ph)_{24}$ (liquid)	Au L_3-edge	3.3*	2.820 ± 0.007	9.7 ± 0.6	Au-S: CN = 1.26*, r = 2.346±0.003	Icosahedral	3–12.5	No	(As above)	MacDonald et al. 2011 [85]
$Au_{38}(SeC_{12}H_{25})_{24}$	Au L_3-edge	1.8 ± 0.8	2.773 ± 0.008	0 ± 22	Au-Se: CN = 1.4 ± 0.2, r = 2.429 ± 0.002	–	3–13.5	Yes	XANES, ESI/ MALDI, TGA, XPS, UV–vis, TEM, XRD	Kurashige et al. [96]
$Au_{38}(SC_{12}H_{25})_{24}$	Au L_3-edge	1.7 ± 0.5	2.747 ± 0.005	7 ± 12	Au-S: CN = 1.6 ± 0.2, r = 2.319 ± 0.003	–	3–13.5	Yes	(As above)	Kurashige et al. 2013 [97]
$Au_{38}(SC_{12}H_{25})_{24}$	Au L_3-edge	1.7 ± 0.2	2.791 ± 0.006	2 ± 3	Au-S: CN = 1.4 ± 0.1) , r = 2.342 ± 0.006	–	3-13	No	Maldi, TEM,XPS, UV–vis, XRD	Nishigake et al. 2012 [147]

$Au_{41}(S\text{-}Eind)_{12}$	Au L_3-edge	4.1 ± 0.4	2.720 ± 0.005	12 ± 5	Au-S: CN = 0.9 ± 0.4, r = 2.353 ± 0.005	–	3-13	No	(As above)	Nishigake et al. 2012 [147]
$Au_{55}(PPh_3)_{12}Cl_6$ (8 K)	Au L_3-edge	7.8 ± 1	2. 803 + 0.01	5.7	AuCl: CN = 0.2 ± 0.2, r = 2.31 ± 0.1	–	2.5–16.5	No	XANES	Marcus et al. 1990 [71]
$Au_{55}(PPh_3)_{12}Cl_6$	Au L_3-edge	6.5 ± 0.4	2.785 ± 0.003	–	–	Face-centered cubic	2-18	Yes	XANES, UV–vis, WAXS	Benfield et al. 2001 [10]
$Au_{55}(PPh_3)_{12}Cl_6$ (two samples)	Au L_3-edge	7.0 ± 2.5, 7.3 ± 2.5	2.76 ± 0.02, 2.78 ± 0.02	11.5 ± 0.4, 11.0 ± 0.4	–	–	3.5–14.5	Yes	–	Fairbanks et al. 1990 [70]
$Au_{55}(PPh_3)_{12}Cl_6$ (80 K)	Au L_3-edge	7.6 ± 1	2.75 ± 0.01	9.5 ± 0.2	2^{nd} Au-Au: CN = 5.0 ± 8 r = 3.93 ± 0.04	–	–	No	–	Clusky et al. 1993 [69]
					3^{rd} Au-Au: CN = 0.60 ± 0.5 r = 4.88 ± 0.01					
					Au-P: CN = 0.66 ± 0.3, r = 2.30 ± 0.02					
					Au-Cl: CN = 2.3 ± 1, r = 2.50 ± 0.01					
$Au_{55}(PPh_2C_6H_4SO_3Na)_{12}Cl_6$ (80 K)	Au L_3-edge	5.55 ± 0.7	2.79 ± 0.01	8.5 ± 0.1	2^{nd} shell Au-Au: CN = 3.5 ± 4.4, r = 3.97 ± 0.03	–	–	No	–	Clusky et al. 1993 [69]
					3^{rd} shell Au-Au: CN = 1.1 ± 1.2, r = 4.90 ± 0.02					
					Au-P: CN = 0.87 ± 0.6, r = 2.26 ± 0.02					
					Au-Cl: CN = 5.0 ± 3.5, r = 2.47 ± 0.02					

(*continued*)

Table 5.1 (continued)

Nanocluster	EXAFS	1st shell M–M CN	1st shell M–M dist., r (Å)	Disorder param (10^{-3} Å^2)	Other shells, dopant data	Structure	k-range (Å^{-1})	EXAFS fit plot?	Other techniques	Reference
$Au_{55}(T8\text{-}OSS\text{-}SH)_{12}CL_6$	Au L_3-edge	6.3 ± 0.5	2.794 ± 0.003	8.5	–	Face-centered cubic	2-18	Yes	XANES, UV–vis, WAXS	Benfield et al. 2001 [10]
$Au_{55}(PPh_3)_{12}Cl_6$ in Al_2O_3	Au L_3-edge	7 ± 2	2.84 ± 0.01	–	–	Face-centered cubic	2-18	Yes	(As above)	Benfield et al. 2001 [10]
Au_{55}-thiol (size: 10–30 ± 15 Å)	Au L_3-edge	7.5-8.5 ± 1	2.845-2.860 ± 0.005	–	–	Face-centered cubic	2-12	Yes	TEM	Frenkel et al. 2005 [12]
$Au_{144}(SR)_{60}$ (SR = PhC_2H_4S)	Au L_3-edge	7.0 ± 0.4	2.831 ± 0.002	13.8 ± 0.4	Au-S: CN = 0.83 ± 0.06, r = 2.340 ± 0.003	Icosahedral	3–11.7	Yes	XANES, l-DOS, XPS	MacDonald et al. 2010 [93]
Au147@Sn* DEN G6-OH) † containing an average of 147 atoms per particle (Au147), functionalized with 2ME, where n is the number of surface 2ME ligands per particle (thiols/DEN))	Au L_3-edge	N = 0: 8.8 ± 0.9	N = 0: 2.811 ± 0.005	11.9 ± 1.0	–	–	–	Yes	UV–vis, TEM	Yancey et al. 2013 [101]
		N = 12: 8.8 ± 1.4	N = 12: 2.815 ± 0.007	12.7 ± 1.4	Au-S, n = 12: CN = 0.31					
		N = 24: 8.5 ± 1.0	N = 24: 2.822 ± 0.005	13.1 ± 1.0	Au-S, n = 24: CN = 0.46					
		N = 50: 8.0 ± 1.0	N = 50: 2.826 ± 0.005	12.7 ± 1.1	Au-S, n = 50: CN = 0.66					
		N = 72: 6.6 ± 0.9	N = 50: 2.826 ± 0.005	12.7 ± 1.1	Au-S, n = 72: CN = 0.95					

Au_x MPCs (183 ± 116 Au atoms)	Au L_3-edge	SS1 path: 8.9 ± 0.5	SS1 path: 2.83 ± 0.01	13 ± 1	SS2 path: CN = 3 ± 2, r = 4.01 ± 0.02	–	3-12	Yes	XANES, HRTEM, HAADF-STEM	Menard et al. 2006 [3]
				1 ± 1	TR path: CN = 35 ± 18, r = 4.25 ± 0.02					
					SS3 path: CN = 9 ± 3, r = 4.91 ± 0.02					
					Au-S SS1 path: CN = 0.7 ± 0.1, r = 2.310 ± 0.005					
Au_{147}-thiol (size: 20–25 ± 10 Å)	Au L_3-edge	8.5 ± 1	2.855-2.860 ± 0.005	–	–	Face-centered cubic	2-12	Yes	TEM	Frenkel et al. 2005 [12]
Au_{561}-thiol (size: 30–50 ± 15 Å)	Au L_3-edge	10.7 ± 1	2.863-2.875 ± 0.005	–	–	Face-centered cubic	2-12	Yes	(As above)	Frenkel et al. 2005 [12]
$Au_X(SR)_Y$: 2 nm	Au L_3-edge	7 ± 1	2.854 ± 0.008	5.8 ± 0.8	–	Face-centered cubic	3.4–16	No	XANES, TEM	Zanchet et al. 2000 [87]
$Au_X(SR)_Y$: 3.2 nm		6 ± 1	2.862 ± 0.005	2.4 ± 0.5						
$Au_X(SR)_Y$: 4.1 nm		8 ± 1	2.866 ± 0.003	1.6 ± 0.5						
COPPER										
Cu_{13} $(RNH_2)_y$	Cu K-edge	7.3 ± 1.4	2.56 ± 0.04	9.8 ± 1.7	–	Icosahedral	2-14	Yes	XANES, DFT, AFM	Oyanagi et al. 2014 [107]
Cu_{13} $(RNH^-)_y$	Cu K-edge	3.5 ± 0.6	2.56 ± 0.05	7.6 ± 1.3	Cu-N: CN: 0.7 ± 0.3, r = 1.90 ± 0.02	Icosahedral	2-14	Yes	(As above)	Oyanagi et al. 2014 [107]
PALADIUM										
$[Pd_9L(O)_3(OAc)_3]m$ (L = 1 ,10-phenanthroline; m = 63.5 ± 3.5; 570 ± 30 Pd atoms in cluster)	Pd K-edge	–	2.60 ± 0.04	–	2^{nd} Pd-Pd: r = 3.10 ± 0.10	Icosahedral	–	No	XRD, TEM	Vargaftik et al. 1985 [74]
					3^{rd} Pd-Pd: r = 3.66 ± 0.10					
					4th Pd-Pd: r = 4.08 ± 0.10					

(*continued*)

Table 5.1 (continued)

Nanocluster	EXAFS	1st shell M–M CN	1st shell M–M dist., r (Å)	Disorder param (10^{-3} Å^2)	Other shells, dopant data	Structure	k-range (Å^{-1})	EXAFS fit plot?	Other techniques	Reference
$Pd_4(CO)_4(OAc)_4$	Pd K-edge	–	2.64	–	2nd Pd-Pd: r = 2.99 Pd-C: r = 1.92 Pd-O: r = 2.20	Several	–	No	SAXS, TEM, ED, MS, NMR	Vargaftik et al. 1991 [75]
$(Pd_{29}Au_{118})$ DEN (G6-OH) †	Pd K-edge	1 ± 2	2.83 ± 0.07	0 ± 5	–	–	–	Yes	UV–vis	Knecht et al. 2008 [62]
	Au L_3-edge	10 ± 2	2.85 ± 0.07	–						
$(Pd_{29}Au_{118})$ MPC‡	Pd K-edge	–	–	4 ± 5	–	–	–	Yes	(As above)	Knecht et al. 2008 [62]
	Au L_3-edge	7.0 ± 1.5	2.80 ± 0.02	–						
$(Pd_{60}Au_{87})$ DEN (G6-OH) †	Pd K-edge	2.5 ± 1	2.78 ± 0.04	14 ± 11	–	–	–	Yes	(As above)	Knecht et al. 2008 [62]
	Au L_3-edge	8 ± 2	2.84 ± 0.08	–						
$(Pd_{60}Au_{87})$ MPC‡	Pd K-edge	2 ± 2	2.95 ± 0.03	12 ± 3	–	–	–	Yes	(As above)	Knecht et al. 2008 [62]
	Au L_3-edge	8 ± 2	2.77 ± 0.02	–						
$(Pd_{73}Au_{73})$ DEN (G6-OH) †	Pd K-edge	3 ± 2	2.78 ± 0.04	9 ± 6	–	–	–	Yes	(As above)	Knecht et al. 2008 [62]
	Au L_3-edge	6 ± 3	2.84 ± 0.08	–						

$(Pd_{73}Au_{73})$ MPC‡	Pd K-edge	3 ± 2	2.90 ± 0.05	12 ± 3	–	–	–	Yes	(As above)	Knecht et al. 2008 [62]
	Au L_3-edge	7 ± 2	2.75 ± 0.02	–						
$(Pd_{87}Au_{60})$ DEN (G6-OH) †	Pd K-edge	3 ± 1	2.79 ± 0.04	12 ± 2	–	–	–	Yes	(As above)	Knecht et al. 2008 [62]
	Au L_3-edge	7 ± 5	2.85 ± 0.07	–						
$(Pd_{87}Au_{60})$ MPC‡	Pd K-edge	2 ± 2	2.9 ± 0.1	14 ± 2	–	–	–	Yes	(As above)	Knecht et al. 2008 [62]
	Au L_3-edge	7.5 ± 2.0	2.70 ± 0.02	–						
$(Pd_{119}Au_{29})$ DEN (G6-OH) †	Pd K-edge	5 ± 2	2.79 ± 0.04	12 ± 2	–	–	–	Yes	(As above)	Knecht et al. 2008 [62]
	Au L_3-edge	3 ± 2	2.77 ± 0.1	–						
$(Pd_{119}Au_{29})$ MPC‡	Pd K-edge	2 ± 2	2.9 ± 0.1	14 ± 2	–	–	–	Yes	(As above)	Knecht et al. 2008 [62]
	Au L_3-edge	4.5 ± 2.0	2.70 ± 0.02	–						
$Pd_{561}(phen)_{36}O_{200}$	Pd K-edge	–	2.742 ± 0.003	300 K: 7.3 ± 0.3	average CN = 6.8 ± 0.5	Face-centered cubic	2.5–17.5	No	–	Benfield et al. 1995 [72]
			2.743 ± 0.003	190 K: 5.5 ± 0.3						
			2.743 ± 0.003	80 K: 3.7 ± 0.3						

(*continued*)

Table 5.1 (continued)

Nanocluster	EXAFS	1st shell M–M CN	1st shell M–M dist., r (Å)	Disorder param (10^{-3} Å^2)	Other shells, dopant data	Structure	k-range (Å^{-1})	EXAFS fit plot?	Other techniques	Reference
$Pd_{561}(phen)_{36}O_{200}$ (80 K)	Pd K-edge	5.0 ± 0.1	2.73 ± 0.01	4 ± 1	2nd Pd-Pd: CN = 2.0 ± 4, r = 3.83 ± 0.04	–	–	No	–	Clusky et al. 1993 [69]
					3rd Pd-Pd: CN = 2.3 ± 3, r = 4.74 ± 0.02					
					4th Pd-Pd: CN = 1.2 ± 3, r = 5.36 ± 0.03					
Pd7/8 (a ligand-stabilized Pd cluster with 7 or 8 shells)	Pd K-edge	–	300 K: 2.746 ± 0.003	6.6 ± 0.3	average CN = 7.8 ± 0.5	Icosahedral	2.5–17.5	No	–	Benfield et al. 1995 [72]
			190 K: 2.746 ± 0.003	4.7 ± 0.3						
			80 K: 2.747 ± 0.003	3.1 ± 0.3						
Pd_{147} DENs (G6-OH)†	Pd K-edge	8.4 ± 0.6	2.791 ± 0.003	8.4 ± 0.5	–	–	–	Yes	XANES, TEM, XPS, UV–vis	Anderson et al. 2013 [109]
$(Pd_{147}@Cu_{162})$ DENs (G6-OH)†	Pd K-edge	7.8 ± 0.7	2.752 ± 0.005	10 ± 2	Pd-Cu: CN = 1.7 ± 0.9 r = 2.64 ± 0.02	Face-centered cubic	–	Yes	(As above)	Anderson et al. 2013 [109]
PLATINUM										
Pt_{55} DENs (G6-OH)†	Pt L_3-edge	7.4 ± 0.8	–	–	–	–	–	Yes	XANES, TEM, XPS, UV–vis	Pande et al. 2011 [148]
$(Pt_{147}@Pd)$ DENs (G6-OH)†	Pt L_3-edge	10.9 ± 3.7	2.72 ± 0.02	11 ± 4	Pt-Pd: CN = 1.3 ± 00.6 r = 2.72 ± 0.02	Face-centered cubic	–	Yes	XANES, TEM, XPS, UV–vis	Anderson et al. 2013 [109]
	Pd K-edge	4.8 ± 1.1	2.72 ± 0.01	5 ± 1	Pd-Pt: CN = 2.6 ± 1.2 r = 2.72 ± 0.02	Face-centered cubic	–	Yes	(As above)	Anderson et al. 2013 [109]

Pt_{225} DENs (G6-OH)† O_2 exposure	Pt L_3-edge	0.3 V: 6.9 ± 0.5	2.751 ± 0.004	6.4 ± 0.5	Pt-O: CN = 0.7 ± 0.3	Face-centered cubic	3-13	Yes	XANES, TEM, XPS, UV–vis	Myers et al. 2012 [104]
		0.15 V: 7.0 ± 0.5	2.745 ± 0.004	6.0 ± 0.5	Pt-O: CN = 0.5 ± 0.2		3–12.5			
		0.05 V: 7.3 ± 0.4 9.2 ± 1.1	2.734 ± 0.003 2.745 ± 0.007	6.2 ± 0.4 6.7 ± 0.8	Pt-O: CN = 0.4 ± 0.2 Pt-O: CN = 0.5 ± 0.4		3–12.5 3–12.0			
		−0.2 V: 8.1 ± 0.8 8.1 ± 0.6	2.747 ± 0.006 2.740 ± 0.003	6.0 ± 0.7 5.8 ± 0.3	Pt-O: CN = 0.8 ± 0.8 Pt-O: CN = 0.4 ± 0.2		3–12 3-15			
Pt_{225} DENs (G6-OH)† N_2 exposure	Pt L_3-edge	0.3 V: 6.2 ± 0.8	2.752 ± 0.007	6.2 ± 0.4	Pt-O: CN = 0.6 ± 0.3	Face-centered cubic	3-12	Yes	(As above)	Myers et al. 2012 [104]
		0.15 V: 7.0 ± 0.7	2.748 ± 0.005	6.4 ± 0.6	Pt-O: CN = 0.6 ± 0.3		3–12			
		−0.2 V: 8.4 ± 0.6	2.747 ± 0.003	6.5 ± 0.9	Pt-O: CN = 0.5 ± 0.2		3-14			
Pt_{240} DENs (G6-OH)†	Pt L_3-edge	5.8 ± 1.3 (experiment 1)	N/A	N/A	Pt-O: CN = 1.6 ± 0.6 (experiment 1)	N/A	2-11	Yes	XANES, TEM, XPS, UV–vis	Weir et al. 2010 [90]
		9.9 ± 1.1 (experiment 2)			–(experiment 2)					
		10.5 ± 1.5 (experiment 3)			–(experiment 3)					
		8.9 ± 0.9 (experiment 4)			–(experiment 4)					

(*continued*)

Table 5.1 (continued)

Nanocluster	EXAFS	1st shell M–M CN	1st shell M–M dist., r (Å)	Disorder param (10^{-3} Å^2)	Other shells, dopant data	Structure	k-range (Å^{-1})	EXAFS fit plot?	Other techniques	Reference
$Pt_{309}(phen^*)_{36}O_{30}$ (phen* is a sulphonated phenanthroline ligand)	Pt L_3-edge	300 K: 8.0 ± 3	300 K: 2.74 ± 0.03	300 K: 10 ± 1	–	Face-centered cubic	4-18	Yes	XANES	Benfield et al. 1999 [2]
		190 K: 8.0 ± 3	190 K: 2.74 ± 0.02	190 K: 7 ± 1	–					
		80 K: 7.0 ± 3	80 K: 2.74 ± 0.01	80 K: 4 ± 1	2nd Pt-Pt, 80 K: CN = 2.0 ± 1 r = 3.87 ± 0.02					
					3rd Pt-Pt, 80 K: CN = 7.0 ± 3 r = 4.75 ± 0.02					
					4th Pt-Pt, 80 K: CN = 3.0 ± 2 r = 5.46 ± 0.02					

*Value fixed from theory
†Dendrimer-encapsulated nanoparticle
‡Monolayer-protected cluster
€Au and Pt shells not distinguishable

EXAFS spectra can only provide CN, bond distances, and disorder correlations. If a model provides predictions for these values, the validity of the model can be tested.

Specifically for the characterization of APNCs, basic structural models are important tools to determine the structure of the NCs with EXAFS. These models essentially derived from the fcc structure that is inherent to many metals in their bulk form. For their analysis of Au_{55} [10, 70], Pd_{561} [72], and Pt_{309} [2], they used the cuboctahedron (fcc) model and based the verification of the model on the comparison of the CN of the first-shell Me–Me bonding. This method is discussed extensively in Benfield [16] where a formula for the mean CN is derived. For each model system (cuboctahedron (fcc, hcp), icosahedral), the CNs of the atoms in the first shell close to the center atom are distinct. However, in some reports [2, 10, 70, 72], the CNs were always too low compared to the fcc model. The development in the understanding and description of the model system, specifically fcc vs. icosahedral, made it possible to include other features into the analysis. The Me–Me bond distances of the first shell in an icosahedral structure should show splitting of about 0.2 Å into two subshells, but Benfield et al. [10] could not resolve these subshells in their data.

In another early approach, Benfield et al. [2] and Vargaftik et al. [74, 75] used the ratios of the Me–Me distances for the first three shells derived from EXAFS in comparison with these ratios in cuboctahedral and icosahedral models. Vargaftik et al. [75] determine an icosahedral structure for the Pd_{561} cluster they reported, and Benfield et al. [2] reported that the Pt_{309} cluster has fcc structure.

This technique using the CNs of the first shell of the EXAFS analysis comparing to the fcc model was typically used in early EXAFS analyses [12]. Later this technique was expanded to the cubic (fcc) model with different shapes (such as spherical, hemispherical, rod, etc.) [59, 76], to hcp and icosahedral models [73], and to other structures [77]. Figure 5.6 shows the correlation between cluster size and CN of the first nearest neighbor for several structures. The packing structure of these models also implies distinct numbers of atoms in the clusters [16, 78]. An example of these "magic numbers" for a cuboctahedral structure (hcp packing) is shown in Fig. 5.7.

4.1.2 Nanoscale Structural Distortions

Coordination Number Truncation

The coordination number truncation model (CNT) demonstrates that atoms on the surface of the particle are surrounded by fewer neighbors than those in the bulk, and, hence, the average coordination number of the first nearest neighbors decreases [57]. This model was also discussed in Benfield et al. [10] explaining the lower CNs for NCs compared to bulk metal. Using this model, the size of APNCs can be determined by comparison with the coordination numbers of several first shells by assuming specific polyhedral shapes [12]. This CNT method was used by Frenkel [58] for nanoparticles using a hemispherical fcc structure and by Frenkel et al. [12] for APNCs using a spherical fcc structure to determine the cluster size of NCs. More extensive applications of the CNT model including cuboctahedral, icosahedral, and hemispherical cuboctahedral structures by Glasner and Frenkel [73] and pyramidal structures by Beale and Weckhuysen [77] have been reported.

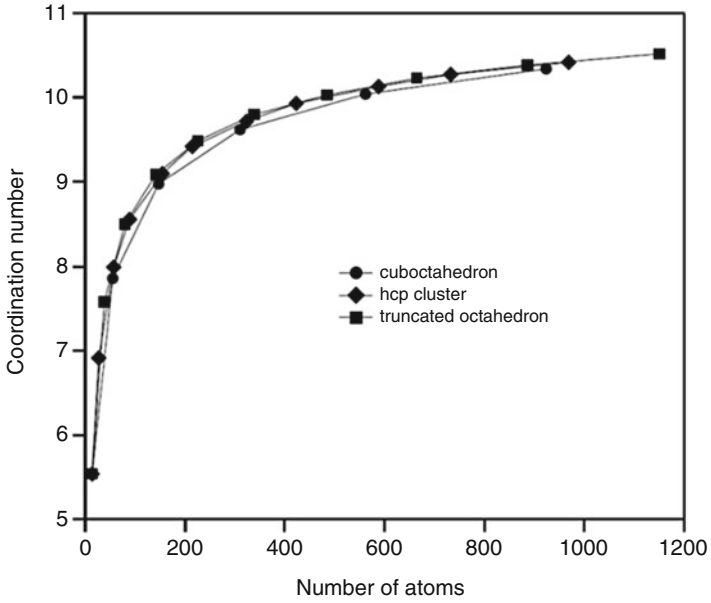

Fig. 5.6 The relation between number of atoms in a cluster and first-shell coordination number for a cuboctahedron, an hcp cluster, and a truncated octahedron (Based on data from Glasner and Frenkel [73])

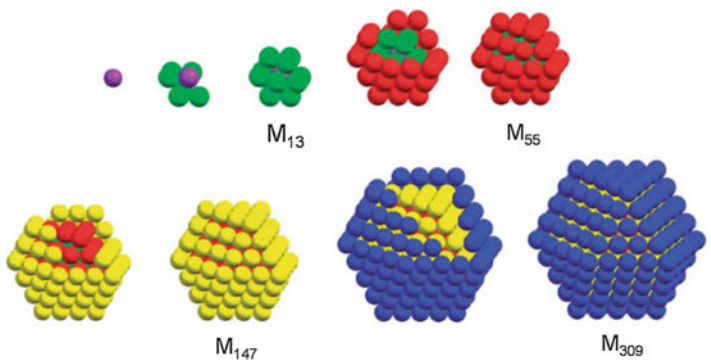

Fig. 5.7 Overview of structures and magic numbers of cuboctahedral clusters of different sizes (Reproduced from Schmid [79] with permission of the Royal Society of Chemistry on behalf of the Centre National de la Recherche Scientifique (CNRS) and the RSC)

Surface Tension

The surface-tension (ST) model was developed by Mays et al. [80]. Here the stress of the surface tension induces compression on the lattice which can be measured (in EXAFS) through the distances of the Me–Me coordination in the first shells if the data for the compressibility K and surface stress f_{rr} are available:

$$d = \frac{4}{3}\frac{f_{rr}K}{\alpha}, \tag{5.10}$$

where d is the particle diameter and $\alpha = \Delta R/R$ is the relative lattice contraction.

Me–Me bond length contraction that is directly related to this lattice contraction was observed not only by Frenkel et al. [12] but previously also by Benfield et al. [2, 10, 72] and Cluskey et al. [69]. Benfield et al. [2] found there to be different contraction rates for Au (4 %), Pt (1 %), and Pd (0.4 %) and related these to the results of differential scanning calorimetry measurements. They observed that bonding for Au–Au in NCs compared to bulk Au is stronger, while for Pd–Pd in NCs bonding is weaker than for bulk Pd. However, it was established by Häberlen et al. [81] and Kruger et al. [82, 83] using DFT calculations that the bond distances in small metal clusters (e.g., Pd, Au) are in direct and nearly linear relation to the mean nearest-neighbor CN and that the bond distances increase with cluster size. Later it was determined that as the particle size increases, the contraction decreases [12]. Further, it was found by Christensen et al. [25] that doping with Pt increased the Au–Au and Au–S contraction in the $Au_{24}Pt(SR)_{18}$ NC compared to the not doped $Au_{25}(SR)_{18}$.

Contraction of the first-shell Au–Au distance was observed by Menard et al. [3] for Au_{13} NCs. The contracted bond length was then used for geometrical calculations in order to determine the bond length of another Me–Me distance in accordance with a structural model, i.e., the distance to the third Au–Au shell which is on the surface of the cluster in an Au_{13} icosahedron. The discrepancies of their model with the experimental data led to the assumption that due to the ligands, there is a relaxation effect and therefore reduced contraction of this third shell distance. One of the objectives of the investigations by Simms et al. [84] was to understand the influence of the thiol ligand structure on the staple motif in Au_{25} NCs and the relationship of this structure toward physiochemical properties. The gigantic bovine serum albumin (BSA) molecule with tertiary structure as a ligand affects the structure of the Au_{25} NCs directly via contraction of the Au–S and Au–Au bonds: The Au–S bonds are shorter than in the theoretical model, while the Au–Au bond lengths agree with the model.

MacDonald et al. [5, 85] studied the effects of temperature and solvation of $Au_{25}(SR)_{18}$ and $Au_{38}(SR)_{24}$ nanoclusters. They observed that although the first two core shells were possibly contracted at lower temperature relative to room temperature, the third shell was expanded. On the other hand, although the nanoparticles solvated in toluene and acetonitrile (ACN) also had the first two core shells contracted, only the nanoparticles solvated in toluene showed an expansion (relaxation), and the Au–Au distance of the third shell solvated in ACN was the same as the solid. The effect that relaxation is sometimes observed for longer Au–Au distances with regard to the ligands is due to surface stabilization [86].

Self-Consistent Analysis

Frenkel et al. [12] were the first to characterize APNCs by applying the two above models (CNT and ST) independently. This self-consistent analysis uses the

comparison of results from two independent methods to give more reliable results than the use of a single model alone when applying a fitting procedure. A spherical fcc structure was used to determine the cluster size for the CNT model. Then, using the EXAFS data from their own experiment and experimentally determined values for f_{rr} and K from the literature, Frenkel and coworkers [12] determined the cluster size of thiol-stabilized gold nanoparticles according to the ST model. These findings by use of the ST model together with EXAFS are in agreement with the works by Zanchet et al. [87] and refined by Zhang and Sham [88] who used the same synthesis method as Frenkel et al. [12] but with different Au/thiol ratios. The work of these three groups did not include specification of the actual numbers of Au atoms determined by other methods such as MALDI-MS and qualify as borderline between studies of regular nanoparticles and studies of specific APNC.

Using these two methods (CNT and ST), Frenkel et al. [12] were able to determine the number of atoms in the core and particle diameters of several thiol-protected very small NCs (close to Au_{55}, Au_{147}, and Au_{561}). The EXAFS results were internally consistent, while the TEM and XRD measurements showed some discrepancies. These differences show that while methods such as TEM and XRD have problems resolving nanoclusters of this size (TEM, poor sensitivity to very small NCs smaller than 2 nm; XRD/Scherrer analysis: When the samples are dispersed in size, higher values for the particle diameter are assumed), this is not the case for EXAFS spectroscopy. However, the size dispersity of the sample does affect the reliability of the EXAFS analysis. The average particle size may be underestimated using the CNT method for size-dispersed samples. This is not the case when the ST model is used because both the mean bond length and its standard deviation (Gaussian distribution, which is the static contribution of the Debye–Waller factor in EXAFS) are involved in the determination of the size [12]. Frenkel et al. [12] concluded that the Au clusters investigated had a cuboctahedral fcc structure (using the CNs of several shells together instead of just the first shell) and that the synthesis methods (with one step or two steps) had an effect on the size of the clusters for the same Au/thiol ratios.

Frenkel and coworkers also used this self-consistent model investigating the geometry of Au_{13} NCs capped with mixed ligands [89]. The EXAFS-derived CN for three shells resulted in an icosahedral structure of the Au_{13} NCs where the number of atoms in the cluster was determined with high-angle annular dark-field scanning transmission electron microscopy (HAADF-STEM). Contraction of Au–Au bonds was measured by EXAFS and compared with ideal icosahedral structures. The differences in contraction (5 % ideal vs. 3 % EXAFS) seem to indicate that a relaxation of the strain is related to the capping ligands [89]. Even though this self-consistent method is very reasonable, it is only not often used.

However, these studies show the importance of using several models for the characterization of APNCs because each method includes some disadvantages.

4.1.3 Synergy of Multiple Techniques: The Use of Complementary Experimental Methods

There are many different techniques for the characterization of materials, such as TEM (transmission electron microscopy), UV–vis (optical spectroscopy), FTIR (Fourier-transformed infrared spectroscopy), XAS, XPS, MALDI-MS (matrix-assisted laser desorption/ionization mass spectrometry), theoretical calculations, and others. It is desirable when possible to use more than one of these techniques for the characterization of APNCs, especially when XRD, which is the major tool for structure determination, is not applicable. In some cases, the different methods complement each other and increase the level of understanding of the system, while in other cases, the results can confirm each other or point out possible problems.

Weir et al. [90] used additional TEM, UV–vis, XPS, and XANES for their in situ EXAFS investigations on Pt_{240} dendrimer-encapsulated nanoclusters (DENs). The details of the in situ EXAFS analysis are discussed in Sect. 4.1.5. UV–vis and TEM results were not discussed as these results were in agreement with previous studies. However, these techniques confirm some properties of the material under investigation. The interrelations of EXAFS with XANES are significant for this analysis. Because the XANES spectra show an oxidized species for one of the experiments, the question of including Pt–O scattering paths in the fitting procedure of the EXAFS analysis can be answered positively. This detail was crucial in the understanding of the effect of the reactions (application to the electrode, with potential, CO adsorption, and CO desorption).

In the work of Simms et al. [84] investigating Au_{25} encapsulated in bovine serum albumin (BSA), a sulfur-rich protein, TEM, EXAFS, XANES, XPS, and l-DOS were used. Here, regular TEM (compared to high-resolution TEM (HRTEM) and HAADF-STEM) is presented and shows one of the drawbacks of this method which is due to the fact that the resolution of the TEM results can be obscured by the enveloping protein. The correlation of XPS, XANES, and l-DOS is discussed in Sect. 4.2. The comparison of these results using different techniques including EXAFS, TEM, and XRD shows that the limitations of the resolution (sizes below 2 nm) of TEM and XRD lead to an overestimation of the cluster size [12]. EXAFS (CNT method) tends to underestimate the size, and EXAFS (ST model) is more accurate [12]. However, TEM can give information about the dispersity of sizes which EXAFS and XRD cannot [12]. In most cases, TEM is employed to monitor the size distribution during a reaction or comparative experiments (e.g., [21, 31]) to observe if the APNCs show changes.

Multiple techniques were used by Menard et al. [3]. To overcome the poor contrast in TEM between the smallest metal nanoparticles and the support films on which they are deposited, high-angle annular dark-field scanning transmission electron microscopy (HAADF-STEM) was employed. Using HAADF-STEM, it was possible to determine the number of atoms in the core as a size distribution showing a homogeneity of the small Au clusters with a *ca.* 13 Au atom core. This information was important to confirm that the EXAFS-derived results of the

coordination numbers had no error. Wrong determination of CNs from EXAFS analysis can arise from a significant presence of other larger clusters (in this case with fcc structure). Due to the precise results from HAADF-STEM, this scenario could be ruled out which again supported that the Au_{13} clusters have icosahedral structure.

Using HRTEM electron diffraction techniques, Menard et al. [3] were able to observe the fcc pseudo-spherical structure of the Au_{147} MPCs, while HAADF-STEM showed a much wider atom number distribution of the core. Detailed modeling showed that the coordination numbers (including CN for Au–S) and distances derived from the EXAFS analysis comply with a truncated octahedral core (which includes that a path for the second single scattering shell is applied). Altogether, in their report, Menard and coworkers [3] show how important are the careful application of models for the EXAFS analysis and the involvement of multiple scattering paths.

Frenkel et al. [89] used the same methodology (HAADF-STEM, TEM, MS EXAFS analysis, and XANES (see Sect. 4.2) as Menard et al. [3] to investigate Au_{13} NCs with a multi-ligand shell. Applying this method, they could characterize the nanocluster sample extensively – since it was both homogeneous in size and of high purity. They determined an icosahedral structure for the Au_{13} clusters, where two thiolates are bound at on-top sites, two thiolates at bridge sites, and four phosphines at on-top sites.

Vargaftik et al. [75] used TEM and SAXS to determine the cluster size of the different Pd NCs investigated. Testing the agglomeration was done with TEM and ED, while NMR, MS, FTIR, and EXAFS were used to determine the structure when XRD was not possible (because no crystal could be grown).

Benfield et al. [10] used wide-angle X-ray scattering (WAXS) as complimentary technique to EXAFS and XANES (which will be discussed in detail in Sect. 4.2) comparing bond distances and crystallite size with the EXAFS-derived results. The results from WAXS measurements are systematically larger than from EXAFS. Longer bond distances (WAXS) can be explained twofold: (a) The WAXS measurements were conducted at room temperatures and EXAFS measurements at 80 K and (b) by aggregation of NCs. The WAXS spectra (being a method similar to XRD) of the NCs are rather broad due to their more amorphous long-range structure.

In other cases [21, 91], the synergetic use of several techniques (Raman, FTIR, MALDI-MS, DFT, HAADF-TEM) was focused on the in situ application of these techniques and will be discussed in Sect. 4.1.5.

4.1.4 Combining EXAFS Analysis with DFT and MD, DFT Modeling Methods, and EXAFS Simulations

EXAFS Simulations on the Basis of DFT-Calculated Structures

Theoretical EXAFS methods, i.e., simulations of EXAFS spectra, are an effective characterization technique. These methods are based on density functional theory (DFT) calculations, and this technique became possible after structural models on the basis of DFT methods of the APNCs $Au_{144}(SR)_{60}$, $Au_{102}(SR)_{44}$, $Au_{38}(SR)_{24}$, and

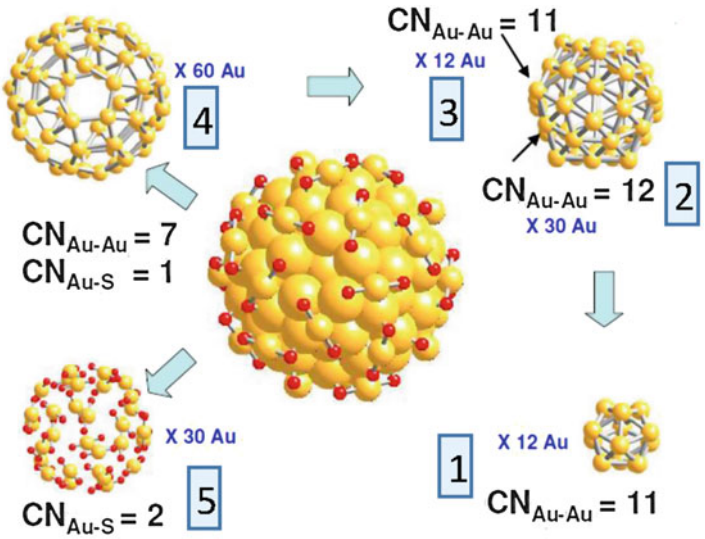

Fig. 5.8 Overview of Au sites (1–5) for the $Au_{144}(SR)_{60}$ NC (Reprinted with permission from MacDonald et al. [93] after Lopez-Acevedo et al. [20]. Copyright 2010 American Chemical Society)

$Au_{25}(SR)_{18}$ were developed by Lopez-Acevedo et al. [20], Jadzinsky et al. [92], Qian et al. [19], and Heaven et al. [18], respectively.

For the Au_{144} cluster, with well-established synthesis practices, MacDonald et al. [93] investigated the agreement of EXAFS in experiment and theory. In the theoretical structure model of the $Au_{144}(SR)_{60}$ cluster, the Au atoms are distinguished with regard to their bonding environment. Lopez-Acevedo et al. [20] proposed that the Au atoms occupy five different sites in this cluster, each of which represents a different environment for the Au atoms within the cluster. The details are shown in Fig. 5.8.

One central feature to the structure of $Au_x(SR)_y$ NCs is the so-called staple motif (Fig. 5.9). Two sulfur atoms of the thiol ligand lift a Au atom up out of the surface of the cluster like in a staple. This was proposed first by Jadzinsky et al. [92]. The staple motif is responsible for the structural stability of $Au_x(SR)_y$ NCs and can occur as monomer (RS–Au–SR) and dimer (RS–Au–(SR)–Au–SR) making Au NCs highly symmetrical [94]. The staple motif model was extended to "staple fitness" by Jiang [15] using combinatorics, and it was observed that the arrangement of the staple motifs on the surface of the NC affects the structure of the core and that the most stable configuration also protects a highly symmetrical core.

Because there are different sites for the Au atoms in the $Au_x(SR)_y$ NCs, theoretical investigations (by MacDonald et al. [93]), which were performed as simulations of EXAFS spectra (in k-space) using this structural information, have to be site specific. This means that for each site, a separate EXAFS spectrum has to be calculated, and these spectra averaged with regard to their number of degeneracy.

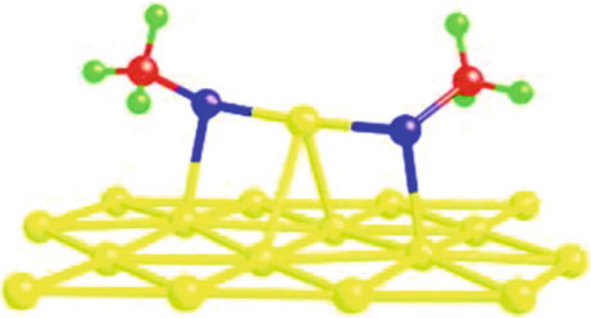

Fig. 5.9 Visualization of the "staple motif" as the thiolate ligand (here R = methanethiol) lifts one Au atom out of the surface (Reprinted with permission from Jiang et al. [94]. Copyright 2008 American Chemical Society)

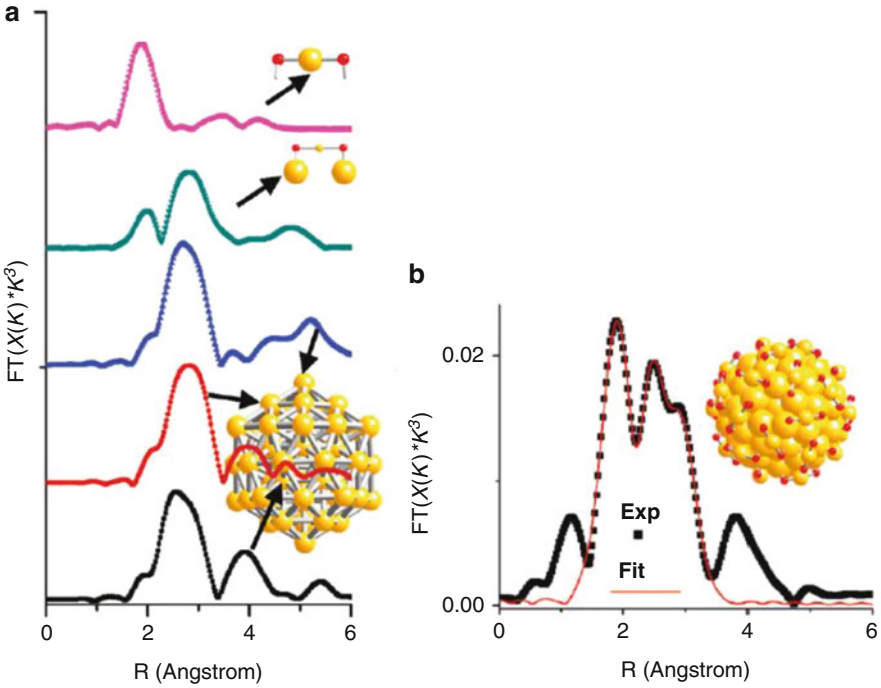

Fig. 5.10 (**a**) Examples of simulated EXAFS spectra for the five different Au sites from *bottom* to *top* (site 1–5) of the $Au_{144}(SR)_{60}$ NC, (**b**) experimental EXAFS spectrum and fit of the $Au_{144}(SR)_{60}$ NC (Reprinted with permission from MacDonald et al. [93]. Copyright 2010 American Chemical Society)

The site-specific EXAFS spectra calculated using this method and the experimental spectrum are shown in Fig. 5.10a. The correlation of the simulated EXAFS spectra with the experimental EXAFS spectra, i.e., $\chi(R)$ in R-space, is an important feature of this work [93]. Clearly, the feature around 2 Å (pink spectrum in Fig. 5.10a) is related to Au–S bonding at site 5 (staple motif), and the next feature (in the other spectra in Fig. 5.10a) at about 2.5 Å is related to the first-shell

Au–Au bonding (e.g., in the core or on the surface). This knowledge is used in all other reports for Au–thiol NCs based on the usual EXAFS fitting methods employing theoretical standards such as metal bulk. However, Fig. 5.10a with the EXAFS simulations showed this effect more visually and directly applied to the NCs. XPS results support this site-specific view of the $Au_{144}(SR)_{60}$ NC where Au atoms in the core show metallic features, Au atoms in the staple show nonmetallic features, and Au atoms on the surface of the NC show mixed features [93]. In addition, these data show that the whole cluster overall exhibits metallic behavior which is supported by the rather high intensity of the Au–Au first-shell peak in the EXAFS spectrum in Fig. 5.10b. Using the model structure of $Au_{102}(SR)_{44}$ [92] for the EXAFS fitting procedure (as standards) gives results for average Au–Au and Au–S CN that agree with the theoretical model of $Au_{144}(SR)_{60}$ from Lopez-Acevedo et al. [20].

Site-specific EXAFS simulations using the structure model of $Au_{25}(SR)_{18}$ cluster, proposed by Qian et al. [19], can show specifically that the first Au–Au shell in the core is split into three subshells. This splitting into subshells is a distinct feature for icosahedral structures, and it was observed in the experimental EXAFS spectra. The EXAFS results of $Au_{25}(SR)_{18}$ for the different environmental conditions show firstly that although the Au–Au bond length for the first Au–Au subshell decreases at low temperature, the Au–Au bond length for the third shell increases. This behavior is also observed in the solvation environments but only for toluene, with no change being observed for acetonitrile. The $Au_{25}(SR)_{18}$ NC is very special compared to the other $Au_x(SR)_y$ NCs. This cluster is characterized by six dimeric staple motifs [5], and these are expected to show significant changes in different solvation environments. For the Au–S bond length, no change can be observed in all cases which means that this stiff SR–Au–SR dimer is less responsive to the changes in the environment making this material (i.e., $Au_{25}(SR)_{18}$) more stable. Secondly, the Debye–Waller factor is much lower at lower temperature (which is to be expected) and also lower for the solvation environment (which is rather unexpected). And thirdly, upon solvation, the structural changes for the Au_{25} are not the same as observed for the Au_{38} cluster. For the Au_{38} cluster, all distances are longer (Au–S and Au–Au), and even splitting of the first Au–Au shell into two subshells for the solvated cluster was observed. The structural changes of Au_{25} are in agreement with the interactions between the aromatic solvent (i.e., toluene) and the ligand tailgroup vs. the polar solvent (i.e., acetonitrile) with the tailgroup. For the second interaction of the polar solvent with the ligand tailgroup, the ligand-induced strain on the core is not reduced as much compared with the results for toluene. There is a relaxation of the Au–Au bond distance in the third shell (and a slight lengthening for Au–S bonds) for the toluene-solvated Au_{25} only compared to the acetonitrile-solvated sample but on the other hand contraction of the first-shell Au–Au bond distance for both solvation environments. These observations confirm that there is an interplay between the Au–S bonding structure in the staple motif and the Au–Au bonding structure in the core [5]. These reports show the capabilities of EXAFS in distinguishing between the different (liquid vs. solid) environmental conditions due to the structural changes that have been observed with regard to tuning the properties of NCs.

Chevrier et al. [95] investigated $Au_{19}(SR)_{13}$ in comparison with $Au_{25}(SR)_{18}$ using EXAFS, XANES, l-DOS, and XPS. Again, XANES, l-DOS, and XPS are discussed in Sect. 4.2. The structure of $Au_{19}(SR)_{13}$ was reported by Jiang [15] (using DFT and XRD methods). Following the above technique of using this structural information from theory, the number of Au atoms in the core was varied in order to understand the structural evolution of NCs and structural stability. First, the EXAFS data were fit using only two shells in order to determine the CN for the Au–S and Au–Au coordination and to identify which of two structural scenarios agrees with the experiment. This step was necessary because the $Au_{19}(SR)_{13}$ cluster was shown to have 11 isomers [15]. Scenario 1 is that the center Au atom has a surface of only ten Au atoms (Au_{11} core) and eight Au atoms coordinate the S atoms in the staple motif (two monomers and three dimers). In scenario 2, the Au_{12} core does not have a center atom, and only seven Au atoms coordinate the S atoms in the staple motif (five monomers and one dimer). The EXAFS fitting procedure of the experimental data agreed better with scenario 1. For the refinement of the structural information, a multishell fitting where the CNs were calculated and fixed based on the $Au_{19}(SR)_{13}$ model (scenario 1) was performed. The Au–S and first Au–Au distance were found to be the same as for Au_{25}, and the second Au–Au distance was a bit longer. While the Au–S and the Au–Au bond distances for the center–surface bonding and surface–surface bonding agree very well with the fit, the long-range aurophilic distances do not. The Au–Au third shell was overestimated (meaning that the fixed CN was too high compared to the experimental data), and an incorrect Debye–Waller factor (being too large) was derived. The comparison with the $Au_{25}(SR)_{18}$ data discussed above shows the differences in the core structure (defective icosahedral) and higher structural disorder especially mixed (monomer and dimer) staple motifs [95]. This report shows that there are limitations of the EXAFS fitting technique in the presence of highly disordered system (in this case only for the long Au–Au bonds), but because of the systematic approach, reasonable conclusions still can be derived.

Exchanging the thiolate ligands for selenolate ligands, the structure of $Au_{25}(SeR)_{18}$ NCs was investigated by Chevrier and coworkers [96] based on the same multishell (three Au–Au shells) approach similar to their previous work discussed above. In addition, the analysis of Se K-edge data was included, which helped enhance the understanding of the Au–Se bond. Also, data on $Au_{25}(SR)_{18}$ were collected, reported, and analyzed again (compare [5]) to ensure consistency, which is very important. A Au–Se distance of 2.42 Å determined by Chevrier et al. was in agreement with the data from Kurashige et al. [97]. The Au–Se distance is longer than for Au–S in $Au_{25}(SR)_{18}$, which is presumed to be due to a larger covalent radius for the Se atom. The temperature dependence of the structure of $Au_{25}(SR)_{18}$ and $Au_{25}(SeR)_{18}$ was studied for 50 and 300 K. Strong contraction for the three Au–Au shells was determined for $Au_{25}(SeR)_{18}$ NCs for 300 K. This negative thermal expansion behavior was supported by DFT calculations (details for DFT calculations are discussed in section "The Relationship of DFT-MD Calculations and DFT Bases EXAFS Calculations"), and it was determined that the angle between the surface and the Au–Se–Au staples as well the angle of Au–Se in the staples changed due to the temperature change [96].

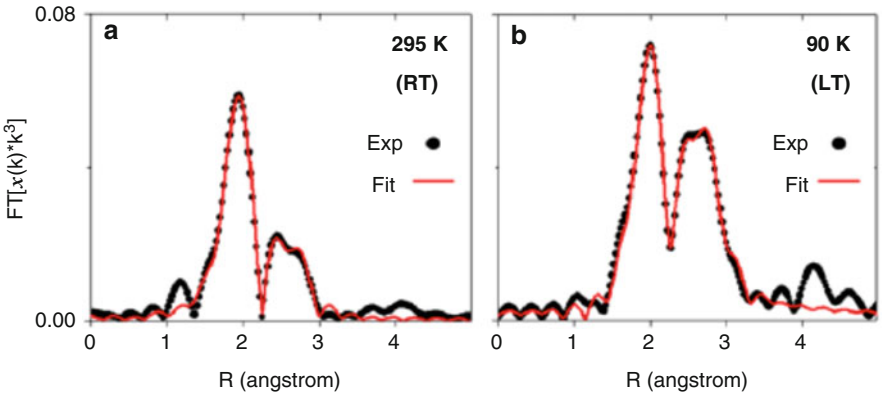

Fig. 5.11 FT-EXAFS data (*black dots*) and fit (*red line*) of the $Au_{36}(SR)_{24}$ NC at (**a**) room temperature and (**b**) low temperature. All peaks in the FT-EXAFS spectrum at low temperature are more intense and well resolved (Reprinted with permission from Chevrier et al. [98]. Copyright 2013 American Chemical Society)

This same EXAFS approach (theoretical model vs. experimental data) was used in the structural determination of $Au_{36}(SR)_{24}$ in comparison with $Au_{38}(SR)_{24}$ by Chevrier et al. [98]. They find that the Au_{36} clusters have an fcc-like core structure and bridging S atoms and four dimeric staple motifs compared to Au_{38} (icosahedral) with only staple motifs. Historically, investigations on the structure of the Au_{36} cluster exist because it is one of the few APNCs that can be grown into crystals and the structure resolved using XRD methods. The fcc-like structure of Au_{36} was verified with EXAFS using a new strategy: From a theoretical model with fcc core structure (Au_{28}), the EXAFS spectrum was simulated (k-space), and then Fourier transformed (R-space) and then backtransformed (k-space) calculated in order to compare this model data with the experimental data (isolated backtransformed signal for Au–Au bonding in the core only). These backtransformed spectra are an astonishingly good match.

Next to the Au–S shell, two Au–Au shells could be determined from the experimental EXAFS analysis. Again the CNs were fixed from the theoretical model, in this case a Au_{28} fcc core with 12 bridging and 8 Au atoms in staple motifs. For the first shell of Au–Au bonding, a much shorter distance compared to the Au_{38} cluster was observed. This experimental EXAFS data (see Fig. 5.11) show how well the scattering peaks at high R (>3.5 Å) are resolved for the low-temperature EXAFS spectra, which is directly correlated to precise (low Debye–Waller factors) values for the bond distances (when the k-range can be extended to about 16 $Å^{-1}$), and that the structural disorder increases quite much for room-temperature measurements (the Debye–Waller factor increases with temperature, and the shells are featured with much lower intensity and broadening in the R-space EXAFS spectra). It also shows that high purity of the samples is crucial for the reliability of the analysis. However, the two different Au–S bonding types (bridging and staple) did not result in different Au–S bond distances in this report [98].

The importance of the Au_4 units for the structure of the fcc-like $Au_{28}(SR)_{20}$ NCs was investigated in comparison with other $Au_x(SR)_y$ NCs in a very recent study by Chevrier et al. [99]. It was shown that site-specific EXAFS simulations can very well agree with experimental EXAFS results.

In another investigation, solely theoretical considerations of Au_{25} and Au_{102} NCs using site-specific EXAFS and l-DOS calculations were reported by Christensen et al. [100]. Due to size differences of the two NCs, the Au–Au coordination environments and also the electronic characters were found to be different. This pure theoretical discussion is important and can lead to valuable information about NC in the transition zone between atomic and bulk materials. In addition to the constant improvement of experimental techniques, the improvement of theoretical techniques is equally important. However, if these theoretical models are not compared with experiment, this information has to be regarded with caution.

The Relationship of DFT-MD Calculations and DFT Bases EXAFS Calculations

In another step to enhance the quality of EXAFS analysis and modeling, Yancey et al. [31] combined them with molecular dynamics (MD) and density functional theory (DFT). In this study, dendrimers were used to synthesize $Au_{147}S_n$ (NC with Au core and thiol shell where n gives Au/thiol ratio, also called thiol capped Au DEN). A similar system (Au–Pt DENs) was discussed in a theoretical way defining the DENs as a model system that is well defined, stable, homogeneous in size, and relatively simple (because they are not on a support) [101]. Yancey et al. [31] used the model system $Au_{147}S_n$ DEN to study the effects of different densities of the thiols on the Au surface (surface ligand density) on the structural disorder of the NCs. Along with EXAFS measurements of the $Au_{147}S_n$ DENs, theoretical EXAFS spectra were calculated based on DFT-MD simulations of the structure of the DENs as well as separate DFT-MD simulations of pair distribution functions (PDF). These methods were also reported by Yevick and Frenkel [102] and Roscioni et al. [103]. The simulated EXAFS spectra were fit using the same modeling strategy as for the experimental EXAFS spectra. More information was included by use of UV–vis and TEM. The size homogeneity was confirmed by TEM for all samples.

The EXAFS analysis shows that the CNs for Au–Au decrease and for Au–S increase when the surface density of thiols increases. This decrease in Au–Au CN with increasing surface density of thiols is in agreement with other results reported for disordered nanoparticle systems (e.g., Myers et al. [104], Price et al. [105]). For the Au–Au distances, a slight increase with higher thiol density was found which relates to a relaxation of the Au–Au bond length as discussed above. On the other hand, the increasing thiol density on the surface results in a decreasing Au–S bond length. This trend is consistent with the existence of the staple motif where the bonding of Au–S is stronger (and thus shorter). If we compare the Au–S bond in a Au–S lattice, the Au–S bond length is longer due to the fact that each S atom is pulling on several Au atoms isotropically (stellate) and vice versa in the three-dimensional lattice. Therefore, a shorter Au–S distance is highly correlated with the formation of staple motif on the surface of the DENs which is more likely for higher Au/thiol ratios. Finally, the Debye–Waller factors increase with increased surface thiol density [31]. The effects of structural disorder are discussed in detail below.

Among their results, Yancey et al. [31] find that using this method, the CNs, average bond lengths, and Debye–Waller factors are in agreement for the theoretical and experimental EXAFS data. Only in the results where the MD-derived parameters from the PDF are compared with the EXAFS-derived parameters (average bond lengths and Debye–Waller factors), there are some discrepancies. The main result of the study is that DFT-MD calculations can simulate complex experimental systems with control over structural disorder in nanoparticles and that this can improve EXAFS fitting methodologies for NC characterization. This combined technique using experimental and theoretical XAS with DFT was also used by Behafarid et al. [106]. Integrating different electron microscope techniques, they characterized Au NCs of different sizes prepared by their new synthesis method employing an inverse micelle encapsulation method with polymers. Distortions of the core structure (e.g., bond length contraction) were found to be size dependent for the ligand-protected NCs. Oyanagi et al. [107] also combined experimental and theoretical XAS with DFT to characterize Cu_{13} NCs synthesized using a new strategy of synchrotron radiolysis together with wet chemistry. Ahmadi et al. [108] also used DFT calculations, in this case on Ag and Cu NCs with cuboctahedral or Marks decahedral structure to determine lattice contraction and coordination. These calculations were though not accompanied by experimental EXAFS results.

4.1.5 In Situ EXAFS

Fast scanning techniques make it possible to observe reactions with EXAFS as they proceed (in situ). The strategic approach of using in situ EXAFS for temperature and extensive catalysis experiments consists of (1) gathering basic structural information about the system using EXAFS and (2) correlating this knowledge with chemical and structural changes of the APNCs during catalytic reactions [21]. UV–vis, MALDI-MS, TEM, and EXAFS together were applied in the examination of $Au_{25}(SR)_{18}$ MPCs on carbon support by Shivhare et al. [21] to determine that heating resulted in the removal of all of the thiolate stabilizers, while cluster integrity was maintained or until higher temperatures. The use of two different ligand thiols (phenylethanethiolate and hexanethiolate) for the experiments showed that higher activity was observed for phenylethanethiolate MPCs. A separate analysis of the $Au_{25}(SR)_{18}$ MPCs on the carbon support confirmed that the cluster kept structural integrity during the transfer process and bond lengths (Au–S and Au–Au) were not temperature dependent. However, the CNs changed (decrease for Au–S, increase for Au–Au bonds). There is a significant increase of the Au–Au CN, and the three Au–Au subshells that are characteristic for the Au_{25} cluster are not separated any longer. This is related to an increase in structural disorder and growth of the clusters, which was confirmed by TEM observing a small growth in the structures with increasing temperatures. Catalytic activation tests were performed with similar experimental conditions showing that the highest catalytic activity were observed at 250 °C where nearly all thiols have been removed from the surface [21].

Wu et al. [91] reported in situ EXAFS on $Au_{25}(SR)_{18}$ supported on CeO_2 including CO oxidation. Other methods used were UV–vis, FTIR, Raman spectroscopy, MALDI-MS, quadrupole-MS, DFT calculations, and HAADF-TEM methods.

While UV–vis, MALDI-MS, and HAADF-TEM were used to confirm the successful synthesis and loading on CeO_2 rods, the CO oxidation treatment was investigated in situ with MS, FTIR, Raman, XAS spectroscopy, and DFT calculations. In this report [91] with huge effort (many techniques) focusing on the CO oxidation effect on the Au_{25} NCs on CeO_2 support, unfortunately, no EXAFS fitting plots and/or table including fitting results were shown or discussed. Even the experimental EXAFS spectra before heating of the Au_{25} NCs on CeO_2 were not discussed. The only focus of the EXAFS analysis was a change in the Au–S bond distance (which did not occur) and the Au–S CN (a decrease was observed with heating). Since no values for Au–Au bonding and no Debye–Waller factors were given, the results derived from this EXAFS analysis can only qualitatively describe the reaction.

The structure of Pt_{240} DENs (on electrode support) during electrocatalytic oxidation of CO was investigated with in situ EXAFS, UV–vis, XPS, and TEM by Weir et al. [90]. UV–vis, XPS, and TEM results were used to confirm either data from previous reports or confirm the XAS data. Using only the CN of the first shell of the EXAFS results, the size of the Pt DENs was estimated to be about 240 atoms in agreement with TEM. After the first application of an electrical potential to the electrode, the Pt DENs were determined to be reduced. Weir et al. [90] observed that the Pt DENs were metallic (reduced) all further reactions. Especially important from this report is that the stability of the Pt DENs was not disrupted during the adsorption and subsequent oxidation of CO. The objective of this study is to understand if the catalyst (Pt DEN) can remain unchanged during the catalysis, which was successfully observed due to the stabilizing effect of the DENs. Immobilization on an electrode prevented agglomeration.

Myers et al. [104] report the in situ investigation of Pt_{225} DENs during electrocatalytic oxygen reduction reaction using EXAFS, XANES, TEM, and UV–vis. They successfully demonstrated the use of an in situ cell (like Weir et al. [90]) for electrometric experiments while recording EXAFS. Applying different potentials and gas conditions, the changes in the structure (Pt–Pt distances and CNs from EXAFS analysis) were observed but could not be fully explained. The structural disorder of the Pt NCs in these experiments can describe the discrepancy of low experimental CN compared to higher theoretical CN (fcc model clusters, size determined by TEM). This correlates well with EXAFS results, specifically multiple scattering contributions, if the core is ordered and the shell disordered. A rather fluid surface behavior for APNC was proposed by Schmid [11] using NMR techniques. This XAS cell and experimental method is promising for the analysis of such in situ experiments using EXAFS analysis. However, better quality and repeatable data is important which can be achieved by repeating measurements at the same conditions in order to make use of the correlation of electrical potential with structural effects.

4.1.6 Bimetallic APNCs

Bimetallic APNCs are discussed in Knecht et al. [62]. Using established synthesis procedures, bimetallic NCs were characterized using EXAFS. Here the synthesis employs dendrimers to form alloyed Au–Pd NCs and dodecane thiols for the extraction and stabilization of the NCs to form monolayer-protected clusters

(MPCs). Bimetallic NCs were generated in different Au/Pd ratios. EXAFS analysis is used to understand the structural changes before and after extraction for all (5) Au/Pd ratios. In their EXAFS analysis, the model for bimetallic NPs (see Sect. 3.3) was applied. Increasing CNs for Pd with increasing Pd concentration for the Au–Pd DENs show that these NCs are partly random alloy and partly in a core–shell structure (with Au in the core and Pd in the shell). For the Au–Pd MPCs, the CNs change drastically, which indicate a clear core–shell structure, where the Pd shell thickness increases with increasing Pd concentration. Additionally, coordination with sulfur was only observed for Pd atoms unless the Pd concentration was very low ($Au_{118}Pd_{29}$). However, the coordination numbers found for Pd–S bonding were much higher than anticipated for the NC model. This indicates the presence of small Pd–thiol complexes as a result of the high excess of thiol addition in the synthesis. The distances for the Au–Au, Pd–Pd, and Au–Pd bonds in the Au–Pd DENs are in agreement with other examples of binary alloys. However, for the Au–Pd MPCs, some distances (Pd–Pd) show some anomalous behavior. This behavior is either caused by relaxation effects in the Pd–S shell or due to misinterpretation cause by the presence of small Pd–S complexes that were found earlier. Detailed interpretation of UV–vis spectra supports the transformation of Au–Pd DENs into Au–Pd MPCs including the formation of a Pd–thiol compound. The analysis of bimetallic EXAFS spectra is very challenging not only because of the higher structural disorder of the system but also because these syntheses often involve the formation of a thiol species that masks the results of the bimetallic sample.

Anderson et al. [109] using in situ EXAFS, complemented by DFT calculations, XPS, UV–vis, XANES, and HRTEM and electrochemical experiments, monitored the three-step synthesis of DENs: (1) formation of a Pd core (Pd_{147} DEN), (2) deposition of a Cu shell ($Pd_{147}Cu_{162}$), and (3) galvanic exchange of Pt for Cu in the shell ($Pd_{1147}Pt_{162}$). The summarized result of this synthesis is instead structural inversion: The DENs with Pd–Cu core–shell structure change into a Pt-rich core and Pd-rich shell structure (Pt_{147} (core) $Pd_{147}Pt_{15}$ (shell)). DFT calculations were employed to help determine the structure of the Pt_{147} (core) $Pd_{147}Pt_{15}$ (shell) DENs after step 3.

Another approach based on site-specific structural considerations (such as in section "The Relationship of DFT-MD Calculations and DFT Bases EXAFS Calculations") can only be applied on very small NCs with only one doping atom. Investigations on $Au_{24}Pt(SR)_{18}$ are reported by Christensen et al. [25] using EXAFS, XPS, and l-DOS. The clusters were analyzed using Pt and Au L_3-edge EXAFS as well as previously published experimental data and theoretical knowledge about $Au_{25}(SR)_{18}$. The analysis of Au L_3-edge EXAFS spectra of the bimetallic cluster showed the contraction of Au–S and Au–Au bond distances in comparison with previous Au_{25} data. Using the Pt L_3-edge EXAFS data, the location of the doped Pt atom was determined to be in the center of the Au_{13} core. The presence of a second Pt species was determined by XPS compositional analysis. This unreacted Pt–thiolate oligomer present in the sample was also observed in the Pt L_3-EXAFS spectrum and causes a very intense Pt–S peak compared to the Pt–Au peak. This would not be possible for Pt in the center of an Au core. Further, while MALDI-MS

can in theory be a great tool to determine the cluster composition, a drawback here is that the Pt–S compound was not detected with MALDI-MS because the molecular mass of this compound was below the detection range of this device. In order to resolve this issue, instead of purifying the sample (which may not possible), Christensen et al. [25] used a theoretical approach to determine the possible CN for this mixture and, therefore, the position of the Pt atom within the Au cluster. Even though the EXAFS analysis was performed without the constraints for bimetallic clusters (as described in Sect. 3.3) and a short k-range only up to 8.8 $Å^{-1}$ (which prevented them from resolving Au–Au vs. Au–Pt distances), this report shows that by use of several complementary methods, reasonable information for a complicated system can be derived.

Site-specific EXAFS simulations together with Mössbauer and EXAFS spectroscopy were used by Negishi et al. [28] in their report of bimetallic $Au_{24}Pd(SR)_{18}$ NC. Only EXAFS measurements at Pd K-edge are reported so only Pd–Au bonding can be discussed. The comparison of experimental with simulated EXAFS spectra of this cluster for Pd at different sites (center of the core, surface, staple) and the very high Pd–Au CN support the notion that the Pd atom is found mainly in the center of the core of the cluster. While no fits for the EXAFS analysis are shown (and the reported *R*-factor is 10 %, which is too high), this group makes an effort to determine the degree of purification of the synthesized clusters and improve the synthesis until the sample is purified. These findings show that effective use of EXAFS can give clear results even for the more complicated bimetallic system if great care is taken in confirming the purity of the sample and good EXAFS measurements.

4.1.7 EXAFS Analysis Is Not a Black Box

EXAFS analysis has a steep learning curve which is obvious if one watches the instruction videos or attends an EXAFS training workshop. The fitting technique using the analysis software is not "intuitive." At the same time, it is not enough to just press some buttons and the result is given. In these fast times where too much stress is laid on the number of publications, there seems to be not enough time to learn this technique by training to fit already-understood data. In this following section, a couple of problems are discussed to point out the difficulties of an EXAFS analysis that are rarely discussed.

Variety of Capping Ligands

One problem in the characterization of APNC by applying EXAFS fitting analysis, which is discussed in Menard et al. [3], is related to different and mixed ligands that are used for the stabilization of the NCs. Next to thiols (e.g., [3, 5, 89, 90, [93, 95, 98]), also phosphines [3, 89], acetates [75], selenides [97], and unoxidized tellurates [110] have been used in the literature reviewed. Also, chlorine can act as ligand as well if it is not carefully removed [69–71]. Specifically for the Au_{55} Schmid cluster, the gold atoms can have several different bonding partners in addition to gold (i.e., chlorine, triphenylphosphine, or nothing) [68]. The overview for this rather complex system is given in Table 5.2.

Table 5.2 Overview of Au sites and bonding ligand for the $Au_{55}(PPh_3)12Cl_6$ cluster

Gold site	Occupancy of site	CN
PPH3	12	5
Unbounded surface	24	7
CL	6	8
Central atom	1	12
Second central shell	12	12

Reprinted from Fairbanks [69]. Copyright (1990) with permission from Elsevier

The scattering amplitudes and phases that are calculated from theory (specifically by use of crystal structures of bulk compounds as an input for the FEFF calculations) are equivalent for elements such as P, S, Cl [3], N, C, O [90], and other elements that have similar atomic masses. The basis of the EXAFS single scattering model is that the backscattering of elements with similar atomic masses cannot be resolved within the EXAFS fitting analysis. This is connected to the principle of transferability of photoelectron phase shifts [111]. In the everyday typical EXAFS analysis, this means that a theoretical compound such as Au_2S can serve as a joint model for the determination of, for example, S and P contributions together or by themselves. It also means that S and P contributions cannot be separated. A complicated set of sites such as the Au_{55} NCs with Au–Cl, Au–P, and Au not bound (as in Table 5.2) cannot be completely specified with EXAFS. This is even more true when the surface is rather fluidic (Schmid [11]) causing structural disorder.

The Effect of Structural Disorder

Within the EXAFS data analysis technique as can be seen from the EXAFS equation (Eq. 5.5), structural disorder is parameterized in the form of the Debye–Waller factor (σ^2) (e.g., Calvin [45]). This total Debye–Waller factor includes thermal dynamic and static components that in turn represent changes in the configuration of the metal and ligand atoms in the NCs with time due to size dispersity [12]. EXAFS is only able to derive results for bond distances and bond length disorders from accurate structural and dynamic characteristics if the underlying distribution is quasi-Gaussian [31]. The effect of increased structural disorder for high temperatures as compared to low temperatures is discussed in Benfield et al. [2, 72], Chevrier et al. [98], and Shivhare et al. [21], specifically employing low temperatures (80 K). However, only in some cases, lower values for the Debye–Waller factor at low temperatures are reported [2, 72, 98]. Another aspect of this comparison is that the quality and reliability of the EXAFS analyses can be improved by taking data for the same sample at different temperatures [2, 21, 72]. The reliability of the EXAFS analysis technique can be tested observing certain ranges for the Debye–Waller factor values. For a reliable EXAFS analysis, σ^2 values for Au–Au bonding (most Me–Me bonding) need to be between 0.005 and 0.01 for the first shell and up to 0.02 for higher shells.

The effects of static structural disorder beyond the Gaussian case that are correlated to symmetric bond length distributions in the NCs are due to different bond

lengths in the core and on the surface of the NCs. This feature is called asymmetric bond length or the anharmonicity of the effective pair potential. This is reflected in the third cumulant parameter [3], a parameter included with modern EXAFS analysis software packages. The role of the third cumulant during the fitting procedure is to give an assessment of the significance of anharmonicity [12]. Symmetric bond length distributions are usually observed in bulk materials (i.e., without surface effects).

In the reports by Frenkel et al. [12], Menard et al. [3], and Yancey et al. [31], it was found that the role of the third cumulant was small. The main issue with this finding, addressed by Yancey et al. [31], is that EXAFS spectra provide only averaged information about the structure and dynamics of the environment of all absorbing atoms of the NC. If this "average" configuration is assumed to be the actual configuration, the EXAFS analysis cannot provide correct structural results. Specifically, this means that a broad distribution of sizes, shapes, crystal structures, and states of order will lead to misinterpretation of the EXAFS spectra. This effect of structural disorder on the EXAFS fit results was investigated in detail in the study by Yancey et al. [31]. One main result of this study is that the EXAFS fitting method which is based on the Gaussian bond length distribution is not able to describe highly disordered systems very well. Such systems can be described better in the PDF extracted from DFT-MD calculations, which can be asymmetric. In a report by Price et al. [105], experimental EXAFS and EXAFS simulations were combined with DFT-MD calculations for small Pt NPs in order to determine how the size determination for small NPs is affected by anharmonicity. They modeled the contraction of the surface layer was well as anisotropic disorder. In many cases, the use of the third cumulant, which should address this issue in the EXAFS fitting procedure, is not applicable because the Au–Au and Au–S bonding features (peaks) overlap and mask possible asymmetry. While it seems that this parameter does not "do" anything for some groups, it is important that it is reported together with errors and with a picture of the fit in k- and R-space in order to verify the reliability of the results.

The Importance of the k-Range and the Limitations of the Resolution of EXAFS

The limitations of the resolution of the EXAFS analysis are discussed in the report by Menard et al. [3]. While an EXAFS analysis can deliver results with a resolution of 0.001 Å for bond distances, this depends on the quality of the data measured. The knowledge that can be gathered from the EXAFS analysis can be limited when the k-range that is measured is too short or noise in high k region shortens the k-range. This results in the limitation of the spatial resolution of the EXAFS data (cf. Fig. 5.12). For example, because of the icosahedral structure of the Au_{13} NC, the Au atoms are distributed in two shells closest to the core (i.e., subshells). This multishell or splitting arises from a 5 % difference of the Au–Au distances in the distance range for the first shell [12] and could not be resolved by Menard et al. [3]. However, this group used a trick to overcome this problem: By calculating the ratios of the distances of the different shells (i.e., R_{3NN}/R_{1NN} third shell vs. first shell), the icosahedral structure for Au_{13} NCs and fcc structure for the Au_{147} MPCs

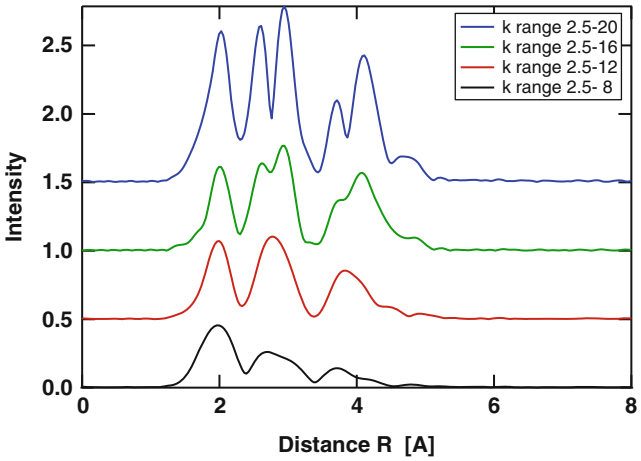

Fig. 5.12 FT-EXAFS spectra in R-space derived from the same EXAFS data (Au–S site in $Au_{102}(SR)_{44}$) for different k-ranges (from *bottom* to *top*, 2.5–8, 2.5–12, 2.5–16, and 2.5–20) (Structural data used from Jadzinsky et al. [92])

could be determined. Additionally, the fact that in the FT-EXAFS R-space spectra no single scattering for a second shell was observed helped with this assessment.

As a positive example where subshells could be observed in the experimental EXAFS spectra, the report by MacDonald et al. [5] is mentioned: The first Au–Au shell in the core is split into three subshells for the $Au_{25}(SR)_{18}$ icosahedron (determined by theoretical EXAFS). There is a discussion about the standardization to report XAS data among the XAFS community (cf. refs: IXS committee [112, 113]) ongoing. However, no agreement has been found yet.

The Requirement of Sample Purity

Menard et al. [3] also discuss discrepancies between the model (truncated octahedron) and the experimental EXAFS results (CN for Au–S) for the Au MPCs they investigated. These discrepancies are possible if the sample contains a thiolate precursor or if the NCs in the sample have degraded. Additional investigations by this group show that there are similarities in the EXAFS data between pure monomer gold (I) thiolate and the thiolate-protected Au MPCs. Menard et al. [3] point out that the EXAFS analysis technique is based on mass-weighted signals (which is nonstatistical). Therefore, with increasing metal cluster size, the CNs increase hyperbolically, and there is a higher sensitivity toward smaller clusters or low-coordination organometallic species. This means that suspiciously high Au–S and low Au–Au scattering magnitudes are related to the presence of a gold (I) thiolate species, making EXAFS uniquely sensitive to this impurity. Menard et al. [3] point out further several reports where the EXAFS data is attributed to pure NC samples; this data is actually identical to the EXAFS data of gold (I) dodecane thiolate and not NCs. The comparison of Au NCs with different cluster size (Au_{144} Au_{38} Au_{25}) by MacDonald et al. [93] confirms the sensitivity of EXAFS to the low-Z

elements because of the quite slow reduction in intensity of the Au–S peak in the EXAFS spectrum of the experimental samples.

The effect of mixed samples on EXAFS analysis is discussed extensively by Frenkel and coworkers, specifically in [55]. The importance (and verification) of the purification of the samples was shown by Negishi et al. [28]. This means that it is important to employ other techniques (e.g., XPS elemental analysis, ICP, EXAFS simulation) to confirm the purity of the sample or that the model applied agrees with the experimental data.

4.2 XANES

4.2.1 Experimental XANES and the Fingerprint Analysis

The measurement of XANES spectra can take less time than the measurement of EXAFS spectra, and more noise is acceptable for the data analysis using the fingerprint method (see Sect. 3.2). In order to gain structural information using the fingerprint method, effort has to be taken to find adequate reference spectra. In the case of APNCs, this is not always possible. In the studies when XANES data of APNCs have been reported, they were mainly shown compared with the bulk metal data (e.g., [28, 71, 84, 91, 93, 114]), which is always measured with the APNC sample simultaneously. Marcus et al. [71] used this comparison to confirm the fcc structure for the Au core in the $Au_{55}(PPh_3)_{12}Cl_6$ NCs since all the features of the bulk metal were observed in the XANES spectrum of the NC. The features (e.g., maxima) in the XANES spectrum were broadened and reduced in intensity which is known to be normal for nanoparticles [9]. Also, in MacDonald et al. [93], the metal character and fcc structure were observed for the $Au_{144}(SR)_{60}$ NCs by comparing the XANES spectra of bulk gold and the NCs. The metallic character of the one Pd atom in the bimetallic cluster $Au_{24}Pd(SR)_{18}$ was observed using Pd K-edge XANES spectra [28].

Another useful approach was reported by Frenkel et al. [89]. They acquired XANES spectra taken from the point of view of the ligand (in this case S and P K-edge) instead of metal core atoms (Au L_3-edge). The change in the chemical environment and, thus, the formation of the Me-ligand bond were confirmed because the features in the XANES spectra (at S or P K-edge) of the $Au_{13}[PPh_3]_4[S(CH_2)_{11}CH_3]_2Cl_2$ NCs were shifted to different energies compared to the pure ligand spectra. This approach was also used by Liu et al. [115]. Using also the ligand "point of view" using S K-edge XANES spectra, the increase in S–Au bonding with increasing cluster size was observed for several Au_xSR_y NCs [93].

Only in the report by Benfield et al. [10], quite a number of reference compounds for Au are presented. This group used the comparison of the XANES fingerprints to determine the metal-like chemical environment and oxidation state of the Au atoms in the $Au_{55}(PPh_3)_{12}Cl_6$ NCs. In addition to the standard reference compounds for the initial solution ($KAuCl_4$), ligand reference (PPh_3AuCl), and bulk gold, several NC and NP are collected in Fig. 5.13 showing how the features of the XANES spectra of the NCs (especially $Au_{55}(PPh_3)_{12}Cl_6$) are broadened as discussed above.

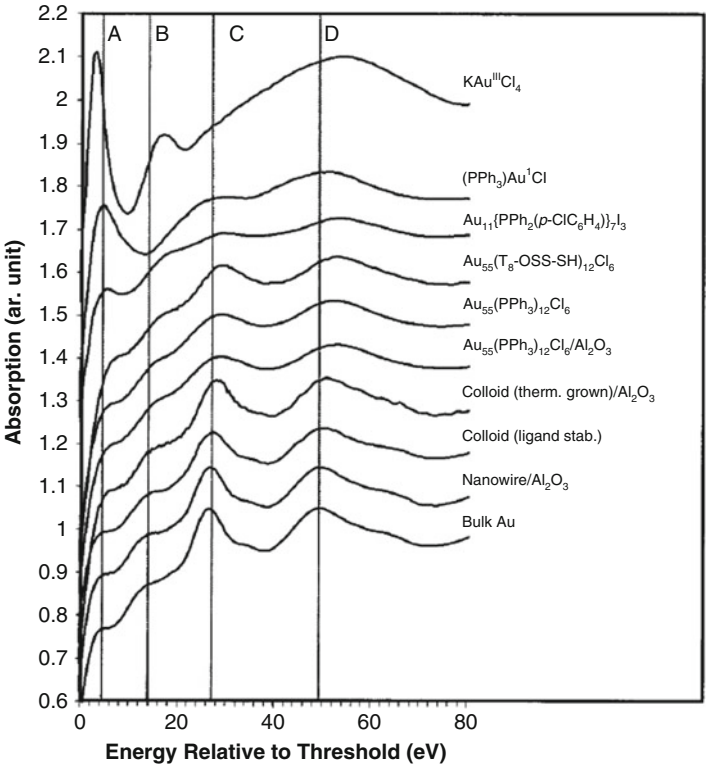

Fig. 5.13 XANES spectra at Au L_3-edge for different Au NP samples and reference compounds (Reprinted with permission from Benfield et al. [10]. Copyright 2001 American Chemical Society)

Even though not precisely about APNCs, Ohyama et al. [116] reported in situ XANES during the formation of (naked) Au NCs. This series of Au L_3-XANES spectra shows how the cluster formation starts with the precursor aurochloric acid (Au^{3+}) after addition of $NaBH_4$, reduction to Au(0), and formation of NP and how aggregation ends with the formation of Au bulk (Fig. 5.14). When the process starts, a broad peak at about 11,929 eV appears (characteristic for KAu(III)Cl) and is reduced in intensity during the reduction. An increase in WL intensity for Au L_3-edge XANES spectra at about 11,929 eV is reported for small NCs [3, 5, 28, 84, 85, 93, 95–98]. This feature is used quite extensively for the analysis of APNCs to determine the catalytic activity. The small difference of the intensity in the Au L_3-edge WL compared to bulk gold is used to indicate an increase in d-hole population.

However, caution must be applied when dealing with small differences. Although experimental XANES spectra are usually less affected by noise (because of the much more intense nature of the WL and SR) than EXAFS spectra, both EXAFS and XANES spectra always contain experimental errors that must be considered when making conclusions from the data. Firstly, there is an experimental error in the

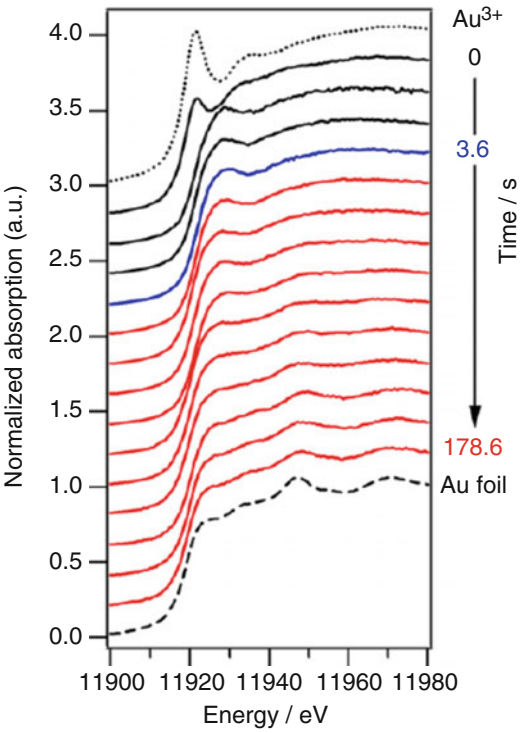

Fig. 5.14 XANES spectra at Au L_3-edge during the formation of Au NPs (Reprinted from Ohyama et al. [116]. Copyright (2011) with permission from Elsevier)

energy (E). If the energetic position of a peak maxima/minima (e.g., WL) or edge E_0 differs by more than the minimum step size (which was used for the measurements), this difference is significant [117]. Therefore, an edge shift of 0.2 eV at Au L_3-edge (11,919 eV) for XANES spectra of two different samples (e.g., at different temperatures) [96] cannot be significant because the minimum step size at Au L_3-edge is at least 0.2 eV (more likely 0.5 eV). Secondly, there is an experimental error in the absorption coefficient (μ) or line intensity. This was discussed in Benfield et al. [2, 10] where the differences in the intensity of the peaks were more than 5 %. An experimental error analysis is always necessary, and this is especially true when trying to make conclusions based on intensity differences of only a few percent. This was crucial, e.g., in the analysis of plant samples by Bovenkamp et al. [118] at Pb L_3-edge using a method to analyze the error contribution to XANES spectra by Bovenkamp et al. [119]. The XAFS community is working toward the implementation of standards for XAS measurements for the last 20 years [112] in order to raise awareness of the effect of the experimental error on the analysis of XAS experiments. If small variations are reported, it should be self-evident to report the error bars of this measurement.

L_3-edge XANES measurements are usually reported for transition metals such as Au and Pt. The L_3-edge XANES spectra for these elements probe the transition $2p \rightarrow 5d_{5/2}$ (or 6 s). Correspondingly, for the L_2-edge, the transition $2p \rightarrow 5d_{3/2}$

(6 s) is probed as discussed in Sect. 3.2. For the transition metals Au and Pt, the $L_{3,2}$-edge spectra are quite sensitive to electronic changes of the d-band which is especially observed in the WL region. These changes directly correlate to the oxidation state and d-band population of the material. In transition metals such as Pt and Au, the 5d-bands are filled in the metal state, and the XANES spectra (at $L_{3,2}$-edges) of these metals do not have a WL. For example, in the case of Au(III) compounds (with oxidation state 3+), the WL increases drastically due to the decrease in the occupancy of the d-orbitals (as d-electrons are transferred to the ligand) (Fig. 5.13: $KAuCl_4$). On the other hand, the Au(I) dodecane-thiolate polymer does not exhibit a strong white line even though the oxidation state of Au is 1+ [3]. This shows that the intensity of the WL does not solely depend on the oxidation state but also on the hybridization of the orbitals [3]. Additionally, stronger d–d interactions in Au NCs that increase the d-charge of Au atoms – as a "nanosize effect" [88] – might result in lower WL intensity compared to that for the bulk. Work by Zhang and Sham [120] shows also a more intense WL for Au NCs capped with thiols compared to capping with weakly interacting dendrimers (the clusters had identical size). The explanation for these effects lies in the difference in charge transfer for Au–S due to the different surface-to-volume ratios for small NCs compared to bigger ones [88] and that the size of the particle does influence this intensity due to broadening [33] as was discussed above.

In order to extract significant information from the shape (e.g., intensity differences of the WL) of the XANES spectrum, several methods intending to estimate densities of unoccupied 5d states around the Fermi level have been developed. These approaches do not just use the comparison of the intensity of the WL per se but the comparison of the intensity of the absorption edge calculated as the area under the peak [121–127]. According to Benfield and coworkers [10], only the method by Mattheiss and Dietz [125] as well as Tyson et al. [127] gives reliable semiquantitative estimates, whereas the others do not. Therefore, in two reports by Benfield et al. [2, 10], a method was used where the L_3-edge and L_2-edge spectra are compared with each other. This method employs the spin–orbit splitting effect between $d_{5/2}$ and $d_{3/2}$ orbitals to gain information on the occupancy of the $d_{5/2}$ orbital. The basis of this method is measurements of L_3-edge XANES spectra of gold, platinum, and iridium by Lytle et al. [128] showing WLs for compounds with metal oxidation state > 0, and band calculation measurements by Mattheiss and Dietz [125] show that spd hybridization causes unoccupied states in the $d_{5/2}$ and $d_{3/2}$ orbitals at the vicinity of the Fermi level.

In Benfield et al. [2], the L_3 to L_2 comparison is used to determine if Pt in the Pt_{309} NCs has molecular (oxidation state > 0) or metallic (oxidation state $= 0$) behavior. For this specific Pt_{309} NC, the comparison of the different area values for Pt foil, K_2PtCl_4, and Pt_{309} NCs resulted in the observation that the Pt atoms in the Pt_{309} NC have metallic character. In their report, Benfield and coworkers [10] investigate the oxidation state of Au in Au_{55} NCs with the same method. However, the area values for the Au_{55} NCs were smaller than those for Au bulk. The small cluster size resulting in stronger d–d interactions was the reason given why this method did not work for gold. This method was not used in any of the later reports. Possibly due to the extra time needed to measure both L_3-edge and L_2-edge XANES.

4.2.2 Theoretical XANES, l-DOS Calculations, and Charge Transfer

In a number of reports [5, 25, 84, 85, 93, 95, 98], mainly on Au APNCs, calculations of the projected DOS and charge transfer of electrons between orbitals have been discussed. The application of l-DOS and charge transfer calculations is useful because the knowledge about the DOS above and around the Fermi level makes it possible to probe the electronic structure dependent on the size of the NCs [3]. L-DOS and charge transfer calculations are used by more researchers because of the development of the theoretical description of XAS ab initio and the FEFF code as a program using those principles.

Without getting into much detail about the theory, which is covered by the literature (e.g., [9, 33, 50]), a short overview is presented here. Version FEFF6 made possible the successful calculation of EXAFS spectra based on single scattering and selected multiple scattering paths. The first time the multiple scattering expansion [129] was used to calculate XANES was in FEFF7, but only with the development of FEFF8 did the self-consistent (SCF) calculations of the scattering potential allow the determination of the Fermi energy and charge transfer. Since version FEFF8 with the development of better algorithms to calculate the matrix elements for the multiple scattering expansion and the development in computer capacity simulations of XANES spectra, l-DOS and charge transfer became easily calculable. Further, the multiple scattering calculations were extended to a real-space full multiple scattering routine [130] to prevent the divergence of the path expansion at low photon energy (which is exactly around the absorption edge). This important feature (real-space full multiple scattering) is crucial in any XANES calculation and, thus, l-DOS and charge transfer calculations. The real-space multiple scattering approach [130], which makes the FEFF8 (and later versions) code so user friendly (i.e., not difficult to use), needs the input of cluster data (of any compound or NC) in real space (xyz). This input can be derived from different atomic programs based on crystal structure.

Using the FEFF code to get a XANES spectrum is not too difficult. However, if something that looks somewhat like (the) data is calculated (and electron counts and l-DOS is calculated in any case), it is important to test its validity. These tests would include:

- Convergence of the SCF calculations (to determine the stability of the Fermi energy and thus electron transfer)
- Convergence of the full multiple scattering calculations (to determine the necessary cluster size)
- Agreement with the experimental data (to determine the validity of the cluster used and thus the l-DOS curves)

For typical compounds, it has been shown that 5–6 shells of atoms around the absorbing atom are required for a multiple scattering calculations in the full multiple scattering module so that the cluster can reproduce a XANES spectrum for that compound [131]. For more complicated structures such as NCs where the cluster size of one particle is effectively too small for the full multiple scattering calculation (e.g., with < 100 atoms in a cluster such as the Au_{25} or Au_{38} NCs), the convergence

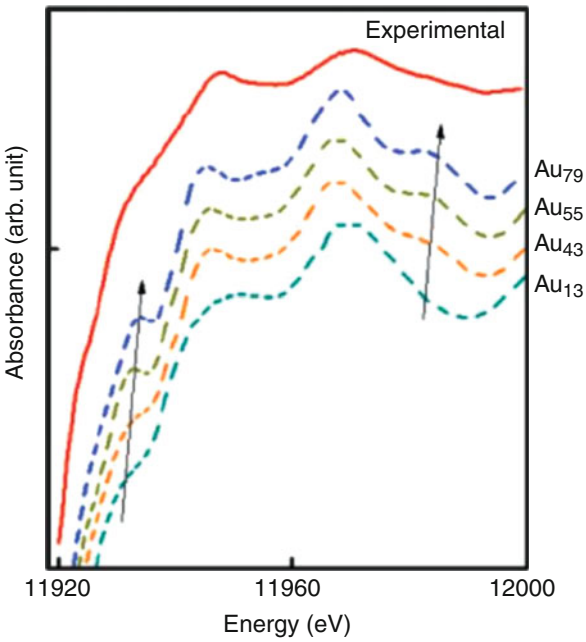

Fig. 5.15 XANES spectra at Au L_3-edge of Au_{13}, Au_{43}, Au_{55}, and Au_{78} clusters calculated with FEFF (Reprinted with permission from Chen et al. [133]. Copyright (2007) American Chemical Society)

of the full multiple scattering calculations cannot be reached which means that the calculated XANES spectrum is not correct. This was described by Soldatov et al. [132] for small clusters at the Au L_3-edge.

The development of XANES features for small Au clusters was studied by Chen et al. [133] applying the XANES simulation tool of FEFF8 using a simple model of fcc gold. Figure 5.15 shows the simulated XANES spectra for several Au clusters created by restricting the cluster size for the full multiple scattering calculation (to shells 1–4) in comparison with the experimental XANES spectrum. Broadening washes out the features (e.g., maxima) of the XANES spectra for NCs (and other small nanoparticles, as was discussed above) similar to the effect of the different Au–Au bonding structure for the surface sites on NCs. Further, theoretical XANES investigations of small metal clusters were also done by Bazin and Rehr [1]. They find that the inner structure as well affects the XANES spectrum [1].

However, in the above report by Chen et al. [133], the XANES calculations are not completely correct, since the cluster size used was too small. The application of the full multiple scattering module, which is crucial for the XANES calculations, involves the inclusion of all multiple scattering contributions. Together with the muffin tin approximation, the center of the potential calculations, it is necessary to use large clusters for the calculations where the contributions of surface atoms can be neglected [1]. For a small cluster, this means that the contributions of (a) the Au–S staple motif atoms and (b) other nearby clusters have to be included.

There are discrepancies between experiment and FEFF calculations that are due to approximations. This fact is known, and the need for improvement of the FEFF

code for XANES calculations is discussed by the developers of FEFF (e.g., [130, 134, 135]). Including full potential calculations instead of spherical muffin tin calculations is necessary to accurately model for anisotropic systems. Also, better treatments of inelastic losses, self-energy, many-body corrections, and core–hole effects need to be implemented. These factors are rarely discussed within the community (because they know about it), but the new user might not be aware of these limitations and the connections between XANES and l-DOS. In a sequence of studies by Soldatov and coworkers [136–139], other software codes not using the muffin tin approximation were compared to FEFF for small clusters of Ti, Cu, and Nb. Oyanagi et al. [107] also used other software codes beyond the muffin tin approximation for their time-resolved characterization of radiolysis-irradiated Cu samples. These studies show the above-stated points.

To better understand the following discussions about l-DOS and charge transfer, some basics about Au are mentioned first. The electronic structure of Au was reported by Coulthard et al. [140] and Kuhn and Sham [141]: Due to the configuration of Au (as $[Xe]4f^{14}5d^{10}6s^{1}$), the d-band in metallic Au is nominally full. However, d and non-d (sp) rehybridization is possible and can create d-band holes where the Fermi level is then somewhere in the middle of the d-band 0.4 of the population for Au [88, 125]. Even for alloy formation, this rehybridization showed a significant effect in XPS and XANES [141]. Therefore, the first peak of the Au L_3-edge XANES spectrum (the WL, transition $2p \rightarrow 5d_{5/2}$) is related to the presence of d-holes [125, 140] (see Fig. 5.13) which, in turn, is related to a peak in the d-DOS. However, caution is necessary when interpreting features of the l-DOS curves as contributions to the XANES spectrum; not in all cases mixing (e.g., p–d mixing results in L_3 features [118]) is possible.

MacDonald et al. [5, 85, 93] used EXAFS, XANES, and XPS, and, in addition, l-DOS and charge transfer calculations, to study Au thiolate APNCs. The XANES spectra of the simulations were found to show features similar to those in the experimental spectra (Fig. 5.16a and b). However, it is not discussed why the experimental data shows a better resolution/less broadening compared to the simulations (usually it is reversed, and additional broadening has to be introduced with the simulated spectra). The strong S–Au/S–C (A and B) line in the S K-edge spectrum was inspected further. The l-DOS calculations here confirm that feature A originates from S–Au bonding and feature B originates from S–C bonding. The features a and a' in the simulated spectrum (Fig. 5.16c) are not resolved in the experimental spectrum (Fig. 5.16a). The discussion of similarities between calculated and experimental spectra in relationship to the presence and absence of S–C bonding is quite useful to confirm the bonding-type information reported by Chaudhuri et al. [142] and Zhang and Sham [88].

L-DOS and charge transfer calculations can be complemented with XPS and can extend the understanding of electronic properties [84]. XPS can also support the other results from MacDonald et al. [93] where the d-DOS of Au–S and Au–Au bonding shows the same behavior (molecular/nonmetallic = sharp singlet, metallic = wide doublet). Similar effects were observed by MacDonald et al. [85] for an Au_{38} cluster, by Chevrier et al. [95] for Au_{19} and Au_{25} clusters, and by Simms et al. [84] for Au_{25} clusters.

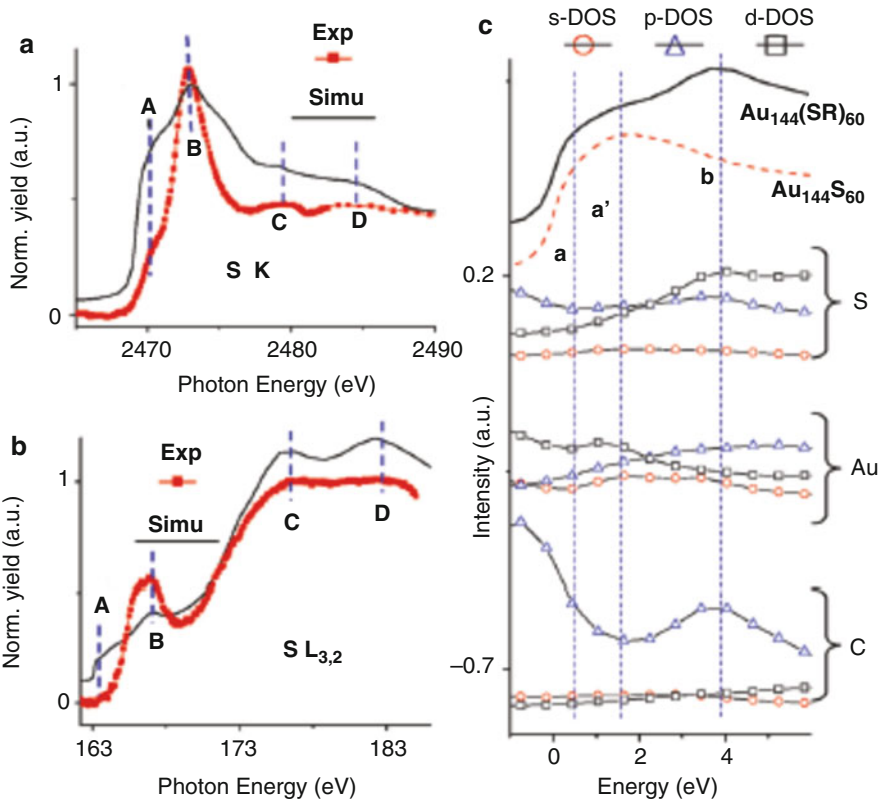

Fig. 5.16 Experimental and theoretical XANES spectra of $Au_{144}(SR)_{60}$ at (**a**) S K-edge, (**b**) S $L_{3/2}$-edge, and (**c**) calculated l-DOS of the S, Au, and C atoms of $Au_{144}(SR)_{60}$, with simulated XANES spectra of $Au_{144}(SR)_{60}$ (*black line*) compared to $Au_{144}S_{60}$ (*red dotted line*), over only about 2470–2476 eV (Reprinted with permission from MacDonald et al. [93]. Copyright 2010 American Chemical Society)

Site-specific d- and s-electron occupancy was used by MacDonald et al. [5, 85] to show similar properties of similar atomic sites for Au_{38} and Au_{25} NCs including charge transfer for Au in staple sites compared to Au in core sites. This is in agreement with a hypothesis of donation (3 s to Au 6 s) and back donation (Au 5d to S 3p) by Park and coworkers [143]. Also in this report, a theoretical model was used to represent solvation effects. The d-DOS curves of both the solid and the modeled (solvated) Au_{38} NC show that next to the narrowing of the d-band in the staple motif (as above) a shift to higher (closer to Fermi level) energies can be observed for the solvated model [85]. This hypothesis should be investigated more closely.

Chevrier et al. [95, 96, 98] compare the l-DOS curves (site specific) of $Au_{19}(SR)_{13}$ vs. $Au_{25}(SR)_{18}$, also $Au_{25}(SeR)_{18}$ vs. $Au_{25}(SR)_{18}$, and Au_{36} vs. ideal Au_{28} core, respectively, similar to the work by MacDonald et al. above. For the

comparison of the Au_{19} vs. Au_{25} NCs, the d-band for Au surface and Au center sites is broadened for Au_{25}. XPS results agree with this observation indicating that the Au_{11} core of Au_{19} has defects and has fewer Au–Au bonding interactions compared to the Au_{13} core of Au_{25} [95]. For the $Au_{25}(SeR)_{18}$ vs. $Au_{25}(SR)_{18}$ NCs, the 5d-band of the selenolate NCs shows higher electron counts compared to the 5d-band of the thiolated NCs which is linked to less charge transfer and more covalent behavior of the Au–Se bond [96]. The investigation of the electronic behavior of $Au_{36}(SR)_{24}$ and $Au_{38}(SR)_{24}$ resulted in the finding that for the Au_{36} cluster, the Au–Au bonding is more molecular compared to a rather metallic Au–Au bonding in Au_{38} NCs [98].

5 Conclusion and Future Perspectives

The quite young field of atomically precise nanoclusters started in the 1980s and was first addressed by the technique of EXAFS in 1985 [74] with early forms of analysis software. The boost of synchrotron radiation facilities and theoretical developments subsequentially has led to greatly improved analysis software and strategies to apply EXAFS to all kinds of systems.

One of the main uses for EXAFS became the determination of the size (number of atoms) of the APNCs. This was implemented using structural models based on atomic packing (e.g., fcc) and the proportionality of size and CN within these models. The successful application of this strategy made it possible to compare TEM, XRD, and EXAFS results.

The EXAFS strategies that were developed for the characterization of NP can be applied similarly to APNCs. However, *improvement*s in EXAFS, such as the CNT model or the surface-tension model, were necessary due to the small size of the NCs. One important feature of all nanoparticle investigations is that the amplitudes of the EXAFS signals (in k-space and R-space) of the nanoparticles compared to the bulk metal are always reduced and in XANES even broadened. It has been shown that a self-consistent approach for the EXAFS analysis, using different models within the same technique, is a good method in order to validify the results characterizing the NCs.

Since XAS is a technique based on the *average configuration* of the sample under investigation, disorder within this configuration (more precisely disorder in the structure due to different bond distances) can lead to EXAFS analysis results that can be misleading.

XANES and EXAFS are not black boxes where a button just has to be pressed to measure the samples and spit out the results. Some understanding of the underlying physics of both methods (which includes an understanding of the errors involved) and a deeper understanding of the methods which are the basis of the technique have to be developed [144].

The techniques and methods that are presented here give a brief overview of the models that EXAFS analysis can use and how XANES and l-DOS calculations can be applied.

The application of complementary techniques (including HRTEM and HAADF-STEM to determine size homogeneity) is important to help validify the EXAFS results. Even more so can theoretical calculations using different techniques (DFT-EXAFS, DFT-MD) help to determine effects of structural disorder on the EXAFS analysis of experimental spectra.

The extraction of electronic information about APNCs from XAS can be done through L-DOS calculations based on FEFF. However, this has to be set in perspective with previous DOS calculations or XPS results to make proper analyses.

In conclusion, we find that a number of groups are using XAS techniques, especially EXAFS analysis for the characterization of APNCs. These reports are not just about understanding the structure of the NCs any longer but more so about tuning the properties of these NCs by varying the ligands. A particular driving force in these reports has been the understanding of the effect of the staple motif. EXAFS is a very powerful tool to study the changes in structure including bond length, coordination environment, and disorder that can be examined very powerfully. This use of the XAS toolbox (theoretical, experimental, in situ EXAFS and XANES, and l-DOS calculations) in its variety does help to gain more accurate information about the structural and electronic properties of APNC and their catalytic application.

Further improvements in the application of EXAFS/XANES in the characterization of APNCs lie in the development of reactors that can be installed in the XAS beamline to collect X-ray absorption spectra in situ as temperature and pressure are varied or other environmental conditions are needed or to observe the synthesis or a catalytic reaction itself. Such reactors to observe the synthesis can be, for example, milli-fluidic reactors (e.g., [145]) which bring the possibility of spatially resolved observation of the reaction. X-ray fluorescence mapping and X-ray microscopy using micro-focused beams are also useful.

Summarizing, we find that EXAFS and XANES are exciting and versatile techniques in the study of APNCs and their use in catalysis. The analysis of XAS data can be quite challenging, however, and it is important to have a thorough knowledge of the physics and possible sources of error involved and, in many cases, combine the EXAFS and XANES analyses with other techniques, and theoretical modeling, to produce the best understanding of the system under investigation.

References

1. Bazin D, Rehr JJ (2003) Limits and advantages of x-ray absorption near edge structure for nanometer scale metallic clusters. J Phys Chem B 107(45):12398–12402. doi:10.1021/Jp0223051
2. Benfield RE, Filipponi A, Morgante N, Schmid G (1999) Structural characterisation of the giant organometallic platinum cluster $Pt_{309}(phen^*)_{36}O_{30}$ using EXAFS. J Organomet Chem 573(1–2):299–304. doi:10.1016/S0022-328x(98)00878-X
3. Menard LD, Xu HP, Gao SP, Twesten RD, Harper AS, Song Y, Wang GL, Douglas AD, Yang JC, Frenkel AI, Murray RW, Nuzzo RG (2006) Metal core bonding motifs of monodisperse icosahedral Au_{13} and larger Au monolayer-protected clusters as revealed by X-ray absorption

spectroscopy and transmission electron microscopy. J Phys Chem B 110(30):14564–14573. doi:10.1021/Jp060740f
4. Zhu M, Aikens CM, Hollander FJ, Schatz GC, Jin R (2008) Correlating the crystal structure of a thiol-protected Au_{25} cluster and optical properties. J Am Chem Soc 130(18):5883. doi:10.1021/ja801173r
5. MacDonald MA, Chevrier DM, Zhang P, Qian H, Jin R (2011) The structure and bonding of $Au_{25}(SR)_{18}$ nanoclusters from EXAFS: the interplay of metallic and molecular behavior. J Phys Chem C 115(31):15282–15287. doi:10.1021/jp204922m
6. Qian HF, Jin RC (2009) Controlling nanoparticles with atomic precision: the case of $Au_{144}(SCH_2CH_2Ph)_{60}$. Nano Lett 9(12):4083–4087. doi:10.1021/nl902300y
7. Schaaff TG, Shafigullin MN, Khoury JT, Vezmar I, Whetten RL (2001) Properties of a ubiquitous 29 kDa Au:SR cluster compound. J Phys Chem B 105(37):8785–8796. doi:10.1021/jp011122w
8. Jin RC (2010) Quantum sized, thiolate-protected gold nanoclusters. Nanoscale 2(3):343–362. doi:10.1039/B9nr00160c
9. Modrow H (2004) Tuning nanoparticle properties – the X-ray absorption spectroscopic point of view. Appl Spectrosc Rev 39(2):183–290. doi:10.1081/Asr-120030955
10. Benfield RE, Grandjean D, Kroll M, Pugin R, Sawitowski T, Schmid G (2001) Structure and bonding of gold metal clusters, colloids, and nanowires studied by EXAFS, XANES, and WAXS. J Phys Chem B 105(10):1961–1970. doi:10.1021/Jp0028812
11. Schmid G (1985) Developments in transition-metal cluster chemistry – the way to large clusters. Struct Bond 62:51–85. doi:10.1007/BFb0009185
12. Frenkel AI, Nemzer S, Pister I, Soussan L, Harris T, Sun Y, Rafailovich MH (2005) Size-controlled synthesis and characterization of thiol-stabilized gold nanoparticles. J Chem Phys 123(18):184701. doi:10.1063/1.2126666
13. Deheer WA (1993) The physics of simple metal-clusters – experimental aspects and simple-models. Rev Mod Phys 65(3):611–676. doi:10.1103/RevModPhys.65.611
14. Hakkinen H, Walter M, Gronbeck H (2006) Divide and protect: capping gold nanoclusters with molecular gold-thiolate rings. J Phys Chem B 110(20):9927–9931. doi:10.1021/Jp0619787
15. Jiang D-e (2011) Staple fitness: a concept to understand and predict the structures of thiolated gold nanoclusters. Chem Eur J 17(44):12289–12293. doi:10.1002/chem.201102391
16. Benfield RE (1992) Mean coordination numbers and the nonmetal metal transition in clusters. J Chem Soc Faraday Trans 88(8):1107–1110. doi:10.1039/Ft9928801107
17. Frenkel A (2007) Solving the 3D structure of metal nanoparticles. Zeitschrift Fur Kristallographie 222(11):605–611. doi:10.1524/zkri.2007.222.11.605
18. Heaven MW, Dass A, White PS, Holt KM, Murray RW (2008) Crystal structure of the gold nanoparticle $[N(C_8H_{17})_4][Au_{25}(SCH_2CH_2Ph)_{18}]$. J Am Chem Soc 130(12):3754–3755. doi:10.1021/ja800561b
19. Qian H, Eckenhoff WT, Zhu Y, Pintauer T, Jin R (2010) Total structure determination of thiolate-protected Au_{38} nanoparticles. J Am Chem Soc 132(24):8280–8281. doi:10.1021/ja103592z
20. Lopez-Acevedo O, Akola J, Whetten RL, Gronbeck H, Hakkinen H (2009) Structure and bonding in the ubiquitous icosahedral metallic gold cluster $Au_{144}(SR)_{60}$. J Phys Chem C 113(13):5035–5038. doi:10.1021/jp8115098
21. Shivhare A, Chevrier DM, Purves RW, Scott RWJ (2013) Following the thermal activation of $Au_{25}(SR)_{18}$ clusters for catalysis by X-ray absorption spectroscopy. J Phys Chem C 117(39):20007–20016. doi:10.1021/jp4063687
22. Myers VS, Weir MG, Carino EV, Yancey DF, Pande S, Crooks RM (2011) Dendrimer-encapsulated nanoparticles: new synthetic and characterization methods and catalytic applications. Chem Sci 2(9):1632–1646. doi:10.1039/C1sc00256b
23. Behrens P (1992) X-ray absorption-spectroscopy in chemistry 2. X-ray absorption near edge structure. TrAC-Trend Anal Chem 11(7):237–244. doi:10.1016/0165-9936(92)87056-P

24. Zhu Y, Qian HF, Drake BA, Jin RC (2010) Atomically precise $Au_{25}(SR)_{18}$ nanoparticles as catalysts for the selective hydrogenation of α, β-unsaturated ketones and aldehydes. Angew Chem Int Ed 49(7):1295–1298. doi:10.1002/anie.200906249
25. Christensen SL, MacDonald MA, Chatt A, Zhang P, Qian H, Jin R (2012) Dopant location, local structure, and electronic properties of $Au_{24}Pt(SR)_{18}$ nanoclusters. J Phys Chem C 116(51):26932–26937. doi:10.1021/jp310183x
26. Negishi Y, Iwai T, Ide M (2010) Continuous modulation of electronic structure of stable thiolate-protected Au_{25} cluster by Ag doping. Chem Commun 46(26):4713–4715. doi:10.1039/C0CC01021A
27. Negishi Y, Igarashi K, Munakata K, Ohgake W, Nobusada K (2012) Palladium doping of magic gold cluster $Au_{38}(SC_2H_4Ph)_{24}$: formation of $Pd_2Au_{36}(SC_2H_4Ph)_{24}$ with higher stability than $Au_{38}(SC_2H_4Ph)_{24}$. Chem Commun 48(5):660–662. doi:10.1039/C1CC15765E
28. Negishi Y, Kurashige W, Kobayashi Y, Yamazoe S, Kojima N, Seto M, Tsukuda T (2013) Formation of a $Pd@Au_{12}$ superatomic core in $Au_{24}Pd_1(SC_{12}H_{25})_{18}$ probed by ^{197}Au Mössbauer and Pd K-edge EXAFS spectroscopy. J Phys Chem Lett 4(21):3579–3583. doi:10.1021/jz402030n
29. Negishi Y, Munakata K, Ohgake W, Nobusada K (2012) Effect of copper doping on electronic structure, geometric structure, and stability of thiolate-protected Au_{25} nanoclusters. J Phys Chem Lett 3(16):2209–2214. doi:10.1021/jz300892w
30. Kurashige W, Munakata K, Nobusada K, Negishi Y (2013) Synthesis of stable Cu_nAu_{25}-n nanoclusters (n = 1–9) using selenolate ligands. Chem Commun 49(48):5447–5449. doi:10.1039/C3CC41210E
31. Yancey DF, Chill ST, Zhang L, Frenkel AI, Henkelman G, Crooks RM (2013) A theoretical and experimental examination of systematic ligand-induced disorder in Au dendrimer-encapsulated nanoparticles. Chem Sci 4(7):2912. doi:10.1039/c3sc50614b
32. Bare SR, Ressler T (2009) Characterization of catalysts in reactive atmospheres by X-ray absorption spectroscopy. Adv Catal 52:339–465. doi:10.1016/S0360-0564(08)00006-0
33. Koningsberger DC, Prins R (1987) X-ray absorption: principles, applications, techniques of EXAFS, SEXAFS, and XANES. Wiley, New York, Chemical analysis, vol. 92
34. Frenkel AI, Cason MW, Elsen A, Jung U, Small MW, Nuzzo RG, Vila FD, Rehr JJ, Stach EA, Yang JC (2014) Critical review: effects of complex interactions on structure and dynamics of supported metal catalysts. J Vac Sci Technol A 32(2) 020801:1–17. doi:10.1116/1.4820493
35. Frenkel AI, Yevick A, Cooper C, Vasic R (2011) Modeling the structure and composition of nanoparticles by extended X-ray absorption fine-structure spectroscopy. Annu Rev Anal Chem 4:23–39. doi:10.1146/annurev-anchem-061010-113906
36. Lapresta-Fernandez A, Salinas-Castillo A, de la Llana SA, Costa-Fernandez JM, Dominguez-Meister S, Cecchini R, Capitan-Vallvey LF, Moreno-Bondi MC, Marco MP, Sanchez-Lopez JC, Anderson IS (2014) A general perspective of the characterization and quantification of nanoparticles: imaging, spectroscopic, and separation techniques. Crit Rev Solid State Mater Sci 39(6):423–458. doi:10.1080/10408436.2014.899890
37. Schmid G (2010) Nanoparticles: from theory to application, 2nd edn. Wiley-VCH, Weinheim
38. Hakkinen H (2008) Atomic and electronic structure of gold clusters: understanding flakes, cages and superatoms from simple concepts. Chem Soc Rev 37(9):1847–1859. doi:10.1039/B717686b
39. Pei Y, Zeng XC (2012) Investigating the structural evolution of thiolate protected gold clusters from first-principles. Nanoscale 4(14):4054–4072. doi:10.1039/C2nr30685a
40. Frenkel AI (2012) Applications of extended X-ray absorption fine-structure spectroscopy to studies of bimetallic nanoparticle catalysts. Chem Soc Rev 41(24):8163–8178. doi:10.1039/C2cs35174a
41. Gao F, Goodman DW (2012) Pd-Au bimetallic catalysts: understanding alloy effects from planar models and (supported) nanoparticles. Chem Soc Rev 41(24):8009–8020. doi:10.1039/C2cs35160a
42. Jin R, Nobusada K (2014) Doping and alloying in atomically precise gold nanoparticles. Nano Res 7(3):285–300. doi:10.1007/s12274-014-0403-5

43. Zhang P (2014) X-ray spectroscopy of gold–thiolate nanoclusters. J Phys Chem C 118 (44):25291–25299
44. Bunker G (2010) Introduction to XAFS: a practical guide to X-ray absorption fine structure spectroscopy. Cambridge University Press, Cambridge/New York
45. Calvin S (2013) XAFS for everyone. CRC press, Boca Raton
46. Kelly SD, Hesterberg D, Ravel B (2008) Analysis of soils and minerals using X-ray absorption spectroscopy. In: Ulery AL (ed) Mineralogical methods. Methods of soil analysis, vol 5. Soil Science Society of America, Madison, pp 387–464
47. Teo BK (1986) EXAFS: basic principles and data analysis. Inorganic chemistry concepts, vol 9. Springer, Berlin/New York
48. Pantelouris A, Kuper G, Hormes J, Feldmann C, Jansen M (1995) Anionic gold in Cs_3auo and Rb_3auo established by X-ray-absorption spectroscopy. J Am Chem Soc 117 (47):11749–11753. doi:10.1021/Ja00152a016
49. Kuno M (2011) Introductory nanoscience – physical and chemical concepts, 1st edn. Garland Science, New York
50. Rehr JJ, Albers RC (2000) Theoretical approaches to x-ray absorption fine structure. Rev Mod Phys 72(3):621–654. doi:10.1103/RevModPhys.72.621
51. Ravel B (2000) Introduction to EXAFS experiments and theory. Open access. doi:http://feff.phys.washington.edu/~ravel/
52. Ravel B, Newville M (2005) ATHENA, ARTEMIS, HEPHAESTUS: data analysis for X-ray absorption spectroscopy using IFEFFIT. J Synchrotron Radiat 12:537–541. doi:10.1107/S0909049505012719
53. Ressler T (1998) WinXAS: a program for X-ray absorption spectroscopy data analysis under MS-Windows. J Synchrotron Radiat 5:118–122
54. Westre TE, Di Cicco A, Filipponi A, Natoli CR, Hedman B, Solomon EI, Hodgson KO (1995) GNXAS, a multiple-scattering approach to EXAFS analysis: methodology and applications to iron complexes. J Am Chem Soc 117(5):1566–1583. doi:10.1021/ja00110a012
55. Frenkel AI, Wang Q, Sanchez SI, Small MW, Nuzzo RG (2013) Short range order in bimetallic nanoalloys: an extended X-ray absorption fine structure study. J Chem Phys 138(6) 064202:1–7. doi:10.1063/1.4790509
56. Calvin S, Carpenter E, Ravel B, Harris V, Morrison S (2002) Multiedge refinement of extended x-ray-absorption fine structure of manganese zinc ferrite nanoparticles. Phys Rev 66(22) 224405:1–13. doi:10.1103/PhysRevB.66.224405
57. Calvin S, Miller MM, Goswami R, Cheng SF, Mulvaney SP, Whitman LJ, Harris VG (2003) Determination of crystallite size in a magnetic nanocomposite using extended x-ray absorption fine structure. J Appl Phys 94(1):778. doi:10.1063/1.1581344
58. Frenkel AI (1999) Solving the structure of nanoparticles by multiple-scattering EXAFS analysis. J Synchrotron Radiat 6:293–295. doi:10.1107/S0909049598017786
59. Frenkel AI, Hills CW, Nuzzo RG (2001) A view from the inside: complexity in the atomic scale ordering of supported metal nanoparticles. J Phys Chem B 105(51):12689–12703. doi:10.1021/Jp012769j
60. Nashner MS, Frenkel AI, Adler DL, Shapley JR, Nuzzo RG (1997) Structural characterization of carbon-supported platinum-ruthenium nanoparticles from the molecular cluster precursor $PtRu_5C(CO)_{16}$. J Am Chem Soc 119(33):7760–7771. doi:10.1021/Ja971039f
61. Frenkel A (2007) Solving the 3D structure of metal nanoparticles. Zeitschrift für Kristallographie 222(11/2007). doi:10.1524/zkri.2007.222.11.605
62. Knecht MR, Weir MG, Frenkel AI, Crooks RM (2008) Structural rearrangement of bimetallic alloy PdAu nanoparticles within dendrimer templates to yield core/shell configurations. Chem Mater 20(3):1019–1028. doi:10.1021/Cm0717817
63. Lemonnier M, Collet O, Depautex C, Esteva JM, Raoux D (1978) High-vacuum two crystal soft-X-ray monochromator. Nucl Instrum Methods 152(1):109–111. doi:10.1016/0029-554x(78)90246-X

64. Lee PA, Citrin PH, Eisenberger P, Kincaid BM (1981) Extended X-ray absorption fine-structure – its strengths and limitations as a structural tool. Rev Mod Phys 53(4):769–806. doi:10.1103/RevModPhys.53.769
65. Stern EA, Kim K (1981) Thickness effect on the extended-X-ray-absorption-fine-structure amplitude. Phys Rev B 23(8):3781–3787. doi:10.1103/PhysRevB.23.3781
66. Boscherini F, de Panfilis S, Weissmuller J (1998) Determination of local structure in nanophase palladium by x-ray-absorption spectroscopy. Phys Rev B 57(6):3365–3374. doi:10.1103/PhysRevB.57.3365
67. Stern EA, Yacoby Y (1996) Structural disorder in perovskite ferroelectric crystals as revealed by XAFS. J Phys Chem Solids 57(10):1449–1455. doi:10.1016/0022-3697(96)00012-1
68. Schmid G, Pfeil R, Boese R, Bandermann F, Meyer S, Calis GHM, Vandervelden WA (1981) $Au_{55}[P(C_6H_5)_3]_{12}cl_6$ – a gold cluster of an exceptional size. Chem Ber 114(11):3634–3642. doi:10.1002/cber.19811141116
69. Cluskey PD, Newport RJ, Benfield RE, Gurman SJ, Schmid G (1993) An EXAFS study of some gold and palladium cluster compounds. Z Phys D At Mol Clusters 26:8–11. doi:10.1007/BF01425601
70. Fairbanks MC, Benfield RE, Newport RJ, Schmid G (1990) An EXAFS study of the cluster molecule $Au_{55}(PPh_3)_{12}Cl_6$. Solid State Commun 73(6):431–436. doi:10.1016/0038-1098(90)90045-D
71. Marcus M, Andrews M, Zegenhagen J, Bommannavar A, Montano P (1990) Structure and vibrations of chemically produced Au_{55} clusters. Phys Rev B 42(6):3312–3316. doi:10.1103/PhysRevB.42.3312
72. Benfield RE, Filipponi A, Bowron DT, Newport RJ, Gurman SJ, Schmid G (1995) EXAFS investigations of high-nuclearity Pd clusters. Phys B Condens Matter 208(1–4):671–673. doi:10.1016/0921-4526(94)00783-R
73. Glasner D, Frenkel AI (2007) Geometrical characteristics of regular polyhedra: application to EXAFS studies of nanoclusters. AIP Conf Proc 882(1):746–748. doi:10.1063/1.2644651
74. Vargaftik MN, Zagorodnikov VP, Stolyarov IP, Moiseev II, Likholobov VA, Kochubey DI, Chuvilin AL, Zaikovsky VI, Zamaraev KI, Timofeeva GI (1985) A novel giant palladium cluster. J Chem Soc Chem Commun 14:937–939. doi:10.1039/C39850000937
75. Vargaftik MN, Moiseev II, Kochubey DI, Zamaraev KI (1991) Giant palladium clusters – synthesis and characterization. Faraday Discuss 92:13–29. doi:10.1039/Fd9919200013
76. Jentys A (1999) Estimation of mean size and shape of small metal particles by EXAFS. Phys Chem Chem Phys 1(17):4059–4063. doi:10.1039/A904654b
77. Beale AM, Weckhuysen BM (2010) EXAFS as a tool to interrogate the size and shape of mono and bimetallic catalyst nanoparticles. Phys Chem Chem Phys 12(21):5562–5574. doi:10.1039/B925206a
78. Teo BK, Sloane NJA (1985) Magic numbers in polygonal and polyhedral clusters. Inorg Chem 24(26):4545–4558. doi:10.1021/Ic00220a025
79. Schmid G (2008) The relevance of shape and size of Au_{55} clusters. Chem Soc Rev 37(9):1909–1930. doi:10.1039/B713631P
80. Mays CW, Vermaak JS, Kuhlmann D (1968) On surface stress and surface tension. 2. Determination of surface stress of gold. Surf Sci 12(2):134. doi:10.1016/0039-6028(68)90119-2
81. Häberlen OD, Chung S-C, Stener M, Rösch N (1997) From clusters to bulk: a relativistic density functional investigation on a series of gold clusters Au_n, n = 6,...,147. J Chem Phys 106(12):5189–5201. doi:10.1063/1.473518
82. Kruger S, Vent S, Rosch N (1997) Size dependence of bond length and binding energy in palladium and gold clusters. Ber Bunsen Phys Chem 101(11):1640–1643. doi:10.1002/bbpc.19971011115
83. Kruger S, Vent S, Nortemann F, Staufer M, Rosch N (2001) The average bond length in Pd clusters Pd_n, n = 4-309: a density-functional case study on the scaling of cluster properties. J Chem Phys 115(5):2082–2087. doi:10.1063/1.1383985

84. Simms GA, Padmos JD, Zhang P (2009) Structural and electronic properties of protein/thiolate-protected gold nanocluster with "staple" motif: a XAS, L-DOS, and XPS study. J Chem Phys 131(21):214703. doi:10.1063/1.3268782
85. MacDonald MA, Zhang P, Chen N, Qian HF, Jin RC (2011) Solution-phase structure and bonding of $Au_{38}(SR)_{24}$ nanoclusters from X-ray absorption spectroscopy. J Phys Chem C 115(1):65–69. doi:10.1021/Jp1102884
86. Fritsche HG, Buttner T (1999) Modification of the lattice contraction of small metallic particles by chemical and/or geometrical stabilization. Z Phys Chem 209:93–101
87. Zanchet D, Tolentino H, Alves MCM, Alves OL, Ugarte D (2000) Inter-atomic distance contraction in thiol-passivated gold nanoparticles. Chem Phys Lett 323(1–2):167–172. doi:10.1016/S0009-2614(00)00424-3
88. Zhang P, Sham T (2003) X-ray studies of the structure and electronic behavior of alkanethiolate-capped gold nanoparticles: the interplay of size and surface effects. Phys Rev Lett 90(24) 245502:1–4. doi:10.1103/PhysRevLett.90.245502
89. Frenkel AI, Menard LD, Northrup P, Rodriguez JA, Zypman F, Glasner D, Gao SP, Xu H, Yang JC, Nuzzo RG (2007) Geometry and charge state of mixed-ligand Au_{13} nanoclusters. AIP Conf Proc 882(1):749–751. doi:10.1063/1.2644652
90. Weir MG, Myers VS, Frenkel AI, Crooks RM (2010) *In situ* X-ray absorption analysis of approximately 1.8 nm dendrimer-encapsulated Pt nanoparticles during electrochemical CO oxidation. Chemphyschem Eur J Chem Phys Phys Chem 11(13):2942–2950. doi:10.1002/cphc.201000452
91. Wu Z, Jiang DE, Mann AK, Mullins DR, Qiao ZA, Allard LF, Zeng C, Jin R, Overbury SH (2014) Thiolate ligands as a double-edged sword for CO oxidation on CeO_2 supported $Au_{25}(SCH_2CH_2Ph)_{18}$ nanoclusters. J Am Chem Soc 136(16):6111–6122. doi:10.1021/ja5018706
92. Jadzinsky PD, Calero G, Ackerson CJ, Bushnell DA, Kornberg RD (2007) Structure of a thiol monolayer-protected gold nanoparticle at 1.1 Å resolution. Science 318(5849):430–433. doi:10.1126/science.1148624
93. MacDonald MA, Zhang P, Qian HF, Jin RC (2010) Site-specific and size-dependent bonding of compositionally precise gold-thiolate nanoparticles from X-ray spectroscopy. J Phys Chem Lett 1(12):1821–1825. doi:10.1021/Jz100547q
94. Jiang DE, Tiago ML, Luo WD, Dai S (2008) The "Staple" motif: a key to stability of thiolate-protected gold nanoclusters. J Am Chem Soc 130(9):2777. doi:10.1021/Ja710991n
95. Chevrier DM, MacDonald MA, Chatt A, Zhang P, Wu Z, Jin R (2012) Sensitivity of structural and electronic properties of gold–thiolate nanoclusters to the atomic composition: a comparative X-ray study of $Au_{19}(SR)_{13}$ and $Au_{25}(SR)_{18}$. J Phys Chem C 116(47):25137–25142. doi:10.1021/jp309283y
96. Chevrier DM, Meng X, Tang Q, Jiang D-e, Zhu M, Chatt A, Zhang P (2014) Impact of the selenolate ligand on the bonding behavior of Au_{25} nanoclusters. J Phys Chem C 118 (37):21730–21737. doi:10.1021/jp508419p
97. Kurashige W, Yamazoe S, Kanehira K, Tsukuda T, Negishi Y (2013) Selenolate-protected Au_{38} nanoclusters: isolation and structural characterization. J Phys Chem Lett 4 (18):3181–3185. doi:10.1021/jz401770y
98. Chevrier DM, Chatt A, Zhang P, Zeng C, Jin R (2013) Unique bonding properties of the $Au_{36}(SR)_{24}$ nanocluster with FCC-like core. J Phys Chem Lett 4(19):3186–3191. doi:10.1021/jz401818c
99. Chevrier DM, Zeng C, Jin R, Chatt A, Zhang P (2014) Role of A_{u4} units on the electronic and bonding properties of $Au_{28}(SR)_{20}$ nanoclusters from X-ray spectroscopy. J Phys Chem C 119 (2):1217–1223. doi:10.1021/jp509296w
100. Christensen SL, Cho P, Chatt A, Zhang P (2014) A site-specific comparative study of Au_{102} and Au_{25} nanoclusters using theoretical EXAFS and l-DOS. Can J Chem 93:1–5. doi:10.1139/cjc-2014-0271

101. Yancey DF, Zhang L, Crooks RM, Henkelman G (2012) Au@Pt dendrimer encapsulated nanoparticles as model electrocatalysts for comparison of experiment and theory. Chem Sci 3(4):1033–1040. doi:10.1039/C2sc00971d
102. Yevick A, Frenkel AI (2010) Effects of surface disorder on EXAFS modeling of metallic clusters. Phys Rev B 81 115451:1–7. doi:10.1103/PhysRevB.81.115451
103. Roscioni OM, Zonias N, Price SWT, Russell AE, Comaschi T, Skylaris C-K (2011) Computational prediction of L_3 EXAFS spectra of gold nanoparticles from classical molecular dynamics simulations. Phys Rev B 83 115409:1–8. doi:10.1103/PhysRevB.83.115409
104. Myers VS, Frenkel AI, Crooks RM (2012) *In situ* structural characterization of platinum dendrimer-encapsulated oxygen reduction electrocatalysts. Langmuir 28(2):1596–1603. doi:10.1021/la203756z
105. Price SWT, Zonias N, Skylaris CK, Hyde TI, Ravel B, Russell AE (2012) Fitting EXAFS data using molecular dynamics outputs and a histogram approach. Phys Rev B 85(7), 075439:1–14. doi:10.1103/Physrevb.85.075439
106. Behafarid F, Matos J, Hong S, Zhang L, Rahman TS, Roldan Cuenya B (2014) Structural and electronic properties of micellar Au nanoparticles: size and ligand effects. ACS Nano 8(7):6671–6681. doi:10.1021/nn406568b
107. Oyanagi H, Orimoto Y, Hayakawa K, Hatada K, Sun Z, Zhang L, Yamashita K, Nakamura H, Uehara M, Fukano A, Maeda H (2014) Nanoclusters synthesized by synchrotron radiolysis in concert with wet chemistry. Sci Rep 4. doi:10.1038/srep07199
108. Ahmadi S, Zhang X, Gong Y, Sun CQ (2014) Effect of atomic under-coordination on the properties of Ag and Cu nanoclusters. Proc SPIE 9165, Phys Chem Interfaces Nanomaterials XIII, 91650. doi:10.1117/12.2059745
109. Anderson RM, Zhang L, Loussaert JA, Frenkel AI, Henkelman G, Crooks RM (2013) An experimental and theoretical investigation of the inversion of Pd@Pt core@shell dendrimer-encapsulated nanoparticles. ACS Nano 7(10):9345–9353. doi:10.1021/Nn4040348
110. Kurashige W, Yamazoe S, Yamaguchi M, Nishido K, Nobusada K, Tsukuda T, Negishi Y (2014) Au_{25} clusters containing unoxidized tellurolates in the ligand shell. J Phys Chem Lett 5 (12):2072–2076. doi:10.1021/jz500901f
111. Citrin P, Eisenberger P, Kincaid B (1976) Transferability of phase shifts in extended X-ray absorption fine structure. Phys Rev Lett 36(22):1346–1349. doi:10.1103/PhysRevLett.36.1346
112. IXS_Committee (2000a) Error reporting recommendation: a report of the International XAFS Society standards and criteria committee. http://ixs.iit.edu/subcommittee_reports/sc/
113. IXS_Committee (2000b) Report of the International XAFS Society standards and criteria committee. http://ixs.iit.edu/subcommittee_reports/sc/
114. Weir MG, Knecht MR, Frenkel AI, Crooks RM (2010) Structural analysis of PdAu dendrimer-encapsulated bimetallic nanoparticles. Langmuir 26(2):1137–1146. doi:10.1021/La902233h
115. Liu J, Krishna KS, Losovyj YB, Chattopadhyay S, Lozova N, Miller JT, Spivey JJ, Kumar CSSR (2013) Ligand-stabilized and atomically precise gold nanocluster catalysis: a case study for correlating fundamental electronic properties with catalysis. Chem-Eur J 19 (31):10201–10208. doi:10.1002/chem.201300600
116. Ohyama J, Teramura K, Shishido T, Hitomi Y, Kato K, Tanida H, Uruga T, Tanaka T (2011) *In Situ* Au L_3 and L_2 edge XANES spectral analysis during growth of thiol protected gold nanoparticles for the study on particle size dependent electronic properties. Chem Phys Lett 507(1–3):105–110. doi:10.1016/j.cplett.2011.03.020
117. Chauvistre R (1987) Absorptionsspektroskopie an Atomen und kleinen Molekülen im weichen Röntgengebiet. Diplom thesis, University of Bonn
118. Bovenkamp GL, Prange A, Schumacher W, Ham K, Smith AP, Hormes J (2013) Lead uptake in diverse plant families: a study applying X-ray absorption near edge spectroscopy. Environ Sci Technol 47(9):4375–4382. doi:10.1021/Es302408m

119. Bovenkamp GL, Prange A, Roy A, Schumacher W, Hormes FJ (2009) X-ray absorption near edge structure spectra as a basis for the speciation of lead. J Phys Conf Ser 190:012190. doi:10.1088/1742-6596/190/1/012190
120. Zhang P, Sham TK (2002) Tuning the electronic behavior of Au nanoparticles with capping molecules. Appl Phys Lett 81(4):736. doi:10.1063/1.1494120
121. Behrens P, Assmann S, Bilow U, Linke C, Jansen M (1999) Electronic structure of silver oxides investigated by AgL XANES spectroscopy. Z Anorg Allg Chem 625(1):111–116. doi:10.1002/(Sici)1521-3749(199901)625:1<111::Aid-Zaac111>3.0.Co;2-7
122. Evans J, Mosselmans JFW (1991) L-edge studies on molybdenum. J Phys Chem 95(24): 9673–9676. doi:10.1021/J100177a015
123. Hlil EK, BaudoingSavois R, Moraweck B, Renouprez AJ (1996) X-ray absorption edges in platinum-based alloys 2. Influence of ordering and of the nature of the second metal. J Phys Chem 100(8):3102–3107. doi:10.1021/Jp951440t
124. Mansour AN, Cook JW, Sayers DE (1984) Quantitative technique for the determination of the number of unoccupied d-electron states in a platinum catalyst using the $L_{2,3}$ X-ray absorption-edge spectra. J Phys Chem 88(11):2330–2334. doi:10.1021/J150655a029
125. Mattheiss LF, Dietz RE (1980) Relativistic tight-binding calculation of core-valence transitions in Pt and Au. Phys Rev B 22(4):1663–1676. doi:10.1103/PhysRevB.22.1663
126. Moraweck B, Renouprez AJ, Hlil EK, Baudoingsavois R (1993) Alloying effects on X-ray absorption edges in $Pt_{1-x}Ni_x$ single-crystals. J Phys Chem 97(17):4288–4292. doi:10.1021/J100119a009
127. Tyson CC, Bzowski A, Kristof P, Kuhn M, Sammynaiken R, Sham TK (1992) Charge redistribution in Au-Ag alloys from a local perspective. Phys Rev B 45(16):8924–8928. doi:10.1103/PhysRevB.45.8924
128. Lytle FW, Wei PSP, Greegor RB, Via GH, Sinfelt JH (1979) Effect of chemical environment on magnitude of x-ray absorption resonance at L_{III} edges. Studies on metallic elements, compounds, and catalysts. J Chem Phys 70(11):4849. doi:10.1063/1.437376
129. Zabinsky SI, Rehr JJ, Ankudinov A, Albers RC, Eller MJ (1995) Multiple-scattering calculations of X-ray-absorption spectra. Phys Rev B 52(4):2995–3009. doi:10.1103/PhysRevB.52.2995
130. Ankudinov AL, Ravel B, Rehr JJ, Conradson SD (1998) Real-space multiple-scattering calculation and interpretation of x-ray-absorption near-edge structure. Phys Rev B 58 (12):7565–7576. doi:10.1103/PhysRevB.58.7565
131. Ravel B (2005) A practical introduction to multiple scattering theory. J Alloy Compd 401 (1–2):118–126. doi:10.1016/j.jallcom.2005.04.021
132. Soldatov MA, Ascone I, Congiu-Castellano A, Messori L, Cinellu MA, Balerna A, Soldatov AV, Yalovega GE (2009) Potential antitumor gold drugs: DFT and XANES studies of local atomic and electronic structure. J Phys Conf Ser 190:012210. doi:10.1088/1742-6596/190/1/012210
133. Chen HM, Liu RS, Asakura K, Jang LY, Lee JF (2007) Controlling length of gold nanowires with large-scale: X-ray absorption spectroscopy approaches to the growth process. J Phys Chem C 111(50):18550–18557. doi:10.1021/Jp0770615
134. Kas JJ, Sorini AP, Prange MP, Cambell LW, Soininen JA, Rehr JJ (2007) Many-pole model of inelastic losses in x-ray absorption spectra. Phys Rev B 76 195116:1–10. doi:10.1103/Physrevb.76.195116
135. Rehr JJ (2006) Theory and calculations of X-ray spectra: XAS, XES, XRS, and NRIXS. Radiat Phys Chem 75(11):1547–1558. doi:10.1016/j.radphyschem.2005.11.014
136. Mazalova V, Kravtsova A, Yalovega G, Soldatov A, Piseri P, Coreno M, Mazza T, Lenardi C, Bongiorno G, Milani P (2007) Free small nanoclusters of titanium: XANES study. Nucl Instrum Methods Phys Res, Sect A 575(1–2):165–167. doi:10.1016/j.nima.2007.01.058
137. Mazalova VL, Soldatov AV, Adam S, Yakovlev A, Möller T, Johnston RL (2009) Small copper clusters in Ar shells: a study of local structure. J Phys Chem C 113(21):9086–9091. doi:10.1021/jp809401r

138. Mazalova VL, Soldatov AV (2008) Geometrical and electronic structure of small copper nanoclusters: XANES and DFT analysis. J Struct Chem 49(1):107–115. doi:10.1007/s10947-008-0208-z
139. Kravtsova AN, Lomachenko KA, Soldatov AV, Meyer J, Niedner-Schatteburg G, Peredkov S, Eberhardt W, Neeb M (2014) Atomic and electronic structure of free niobium nanoclusters: simulation of the $M_{4,5}$-XANES spectrum of Nb_{13}+. J Electron Spectrosc Relat Phenom 195:189–194. doi:10.1016/j.elspec.2014.07.005
140. Coulthard I, Degen S, Zhu YJ, Sham TK (1998) Gold nanoclusters reductively deposited on porous silicon: morphology and electronic structures. Can J Chem 76(11):1707–1716. doi:10.1139/cjc-76-11-1707
141. Kuhn M, Sham T (1994) Charge redistribution and electronic behavior in a series of Au-Cu alloys. Phys Rev B 49(3):1647–1661. doi:10.1103/PhysRevB.49.1647
142. Chaudhuri A, Odelius M, Jones RG, Lee TL, Detlefs B, Woodruff DP (2009) The structure of the Au(111)/methylthiolate interface: new insights from near-edge x-ray absorption spectroscopy and x-ray standing waves. J Chem Phys 130(12) 124708:1–11. doi:10.1063/1.3102095
143. Park YS, Whalley AC, Kamenetska M, Steigerwald ML, Hybertsen MS, Nuckolls C, Venkataraman L (2007) Contact chemistry and single-molecule conductance: a comparison of phosphines, methyl sulfides, and amines. J Am Chem Soc 129(51):15768. doi:10.1021/Ja0773857
144. Ravel B (2014) Deeper understanding of EXAFS. Private communication
145. Krishna KS, Navin CV, Biswas S, Singh V, Ham K, Bovenkamp GL, Theegala CS, Miller JT, Spivey JJ, Kumar CSSR (2013) Millifluidics for time-resolved mapping of the growth of gold nanostructures. J Am Chem Soc 135(14):5450–5456. doi:10.1021/Ja400434c
146. Yu Y, Luo Z, Chevrier DM, Leong DT, Zhang P, Jiang D-e, Xie J (2014) Identification of a highly luminescent $Au_{22}(SG)_{18}$ nanocluster. J Am Chem Soc 136(4):1246–1249. doi:10.1021/ja411643u
147. Nishigaki JI, Tsunoyama R, Tsunoyama H, Ichikuni N, Yamazoe S, Negishi Y, Ito M, Matsuo T, Tamao K, Tsukuda T (2012) A new binding motif of sterically demanding thiolates on a gold cluster. J Am Chem Soc 134(35):14295–14297. doi:10.1021/Ja305477a
148. Pande S, Weir MG, Zaccheo BA, Crooks RM (2011) Synthesis, characterization, and electrocatalysis using Pt and Pd dendrimer-encapsulated nanoparticles prepared by galvanic exchange. New J Chem 35(10):2054–2060. doi:10.1039/C1nj20083f